SANDIA REPORT

SAND2016-9959 Unlimited Release Printed September 2016

Fracture Toughness of Microstructural Gradients

Gustavo M. Castelluccio, Hojun Lim, Corbett C. Battaile and John M. Emery

Prepared by Sandia National Laboratories Albuquerque, New Mexico 87185 and Livermore, California 94550

Sandia National Laboratories is a multi-mission laboratory managed and operated by Sandia Corporation, a wholly owned subsidiary of Lockheed Martin Corporation, for the U.S. Department of Energy's National Nuclear Security Administration under contract DE-AC04-94AL85000.

Approved for public release; further dissemination unlimited.



AND AND

Issued by Sandia National Laboratories, operated for the United States Department of Energy by Sandia Corporation.

NOTICE: This report was prepared as an account of work sponsored by an agency of the United States Government. Neither the United States Government, nor any agency thereof, nor any of their employees, nor any of their contractors, subcontractors, or their employees, make any warranty, express or implied, or assume any legal liability or responsibility for the accuracy, completeness, or usefulness of any information, apparatus, product, or process disclosed, or represent that its use would not infringe privately owned rights. Reference herein to any specific commercial product, process, or service by trade name, trademark, manufacturer, or otherwise, does not necessarily constitute or imply its endorsement, recommendation, or favoring by the United States Government, any agency thereof, or any of their contractors or subcontractors. The views and opinions expressed herein do not necessarily state or reflect those of the United States Government, any agency thereof, or any of their contractors.

Printed in the United States of America. This report has been reproduced directly from the best available copy.

Available to DOE and DOE contractors from

U.S. Department of Energy

Office of Scientific and Technical Information

P.O. Box 62

Oak Ridge, TN 37831

Telephone: (865) 576-8401 Facsimile: (865) 576-5728

E-Mail: reports@adonis.osti.gov
Online ordering: http://www.osti.gov/bridge

Available to the public from

U.S. Department of Commerce National Technical Information Service 5285 Port Royal Rd Springfield, VA 22161

Telephone: (800) 553-6847 Facsimile: (703) 605-6900

E-Mail: orders@ntis.fedworld.gov

Online ordering: http://www.ntis.gov/help/ordermethods.asp?loc=7-4-0#online



SAND2016-9959 Unlimited Release Printed September 2016

Fracture Toughness of Microstructural Gradients

Gustavo M. Castelluccio* and John M. Emery
Component Science and Mechanics,
Sandia National Laboratories, Albuquerque, NM 87185
*gmcaste@sandia.gov - MS 1415

Hojun Lim and Corbett C. Battaile Computational Materials and Data Science, Sandia National Laboratories, Albuquerque, NM 87185

Abstract

Traditional singularity-based fracture mechanics theories rely on their ability to infer the crack tip driving force (local field) by surveying macroscopic physical magnitudes far from the crack tip (far field). This key capability allows engineers to employ nominal forces or displacements to estimate the potential for stable or unstable crack growth. In the case of heterogeneous or anisotropic materials, traditional fracture approaches are not fully theoretically sound and applications rely on extrapolating methodologies with *ad-hoc* corrections.

This Express Laboratory Directed Reseach and Development (ELDRD) program employed mesoscale-sensitive finite element simulations to assess the impact of grain size and texture on the crack tip behavior. A dislocation-based crystal plasticity model conveys grain size effects by computing the constraint on dislocation cell structures. We assessed the effects of microstructural variability on multiple displacement-based measurements of the fracture driving forces for crack opening (Mode I) and sliding (Mode II). We also consider multiple microstructural realizations of single phase metals undergoing ductile failure.

The results show that grain size and texture affect the applied fracture driving force and can induce a significant Mode II deformation under force and displacement control, which is completely neglected in homogeneous models. A large variability in driving forces upon identical far field applied conditions is attributed to a buffering effects of the microstructure. Furthermore, crack mouth opening displacement is almost insensitive to microstructure, which suggests that experimental measurements using such a magnitude (e.g., plastic hinge model) may underestimate local crack tip driving force variability.

Acknowledgment

This work is supported by the Exploratory Express LDRD project 193072, Predicting Performance Margins (PPM) and Advanced Simulation and Computing - Physics and Engineering Models (ASC-P&EM) programs at Sandia National Laboratories.

Sandia National Laboratories is a multi-mission laboratory managed and operated by Sandia Corporation, a wholly owned subsidiary of Lockheed Martin Corporation, for the U.S. Department of Energys National Nuclear Security Administration under contract DE-AC04-94AL85000.

Contents

1	Intr	oduction	9
	1.1	Fundamentals of fracture and microstructure relation	9
2	Mo	deling approaches	11
	2.1	Meshes and microstructures	11
	2.2	Constitutive Model	14
3	Ela	stic dislocation walls	15
	3.1	Constitutive Formulation	15
	3.2	Material parameters and physical constants	17
	3.3	Smooth specimen results	18
	3.4	Results for equiaxed fine microstructures	19
	3.5	Effects on stress and strain fields	22
	3.6	Results for microstructural gradients	25
	3.7	Results for texture gradients	32
4	Pla	stic dislocation walls	37
	4.1	Constitutive Formulation	37
	4.2	Results for equiaxed fine microstructures - Force control	39
	4.3	Results for X-axis texture gradients - Force control	40
5	Dis	cussion and Conclusions	43
	5.1	What is next?	44
R	eferei	nces	44

Figures

1	Crack-tip shielding or amplification of plastic zones that are indicated by the shaded	10
2	areas. (a) crack-tip shielding $J_{tip} < J_{app}$ (b) crack-tip amplification $J_{tip} > J_{app}$	10
2	Finite element mesh in which the boundary conditions represented. The nodes	
	considered for quantifying the crack tip driving forces CTD, CMD, and $\delta 5$ are	12
2	highlighted.	
3	Multiple microstructures employed in the assessment of the crack tip driving force.	13
4	Texture gradients a long different axis. Colors refer schematically to the linear	12
_	varitation of the three Euler angle orientations.	13
5	Constitutive responses of smooth specimens assuming elastic dislocation structures.	19
6	Δ CMD, Δ CTD, and $\Delta\delta$ 5 for multiple equiaxed microstructural realizations under displacement control. Colors represent different microstructural realizations	
	der displacement control. Colors represent different microstructural realizations.	20
7	Black correspond to homogeneous J2 model.	20
7	Δ CMD, Δ CTD, and $\Delta\delta$ 5 for multiple equiaxed microstructural realizations under	
	force control. Colors represent different microstructural realizations. Black corre-	0.1
0	spond to homogeneous J2 model.	21
8	Boxplots summarizing normalized distributions of maximum Δ CMD, Δ CTD, and	22
0	$\Delta \delta 5$ values for multiple equiaxed microstructural realizations under force control.	22
9	Effect of grain size on strain fields under displacement control for $5\mu m$ (left) and	00
10	$100\mu m$ (right) mean grain sizes.	23
10	Effect of grain size on von Misses stress fields under displacement control for $5\mu m$	22
11	(left) and $100\mu m$ (right) mean grain sizes.	23
11	Effect of grain size on strain fields under force control for $5\mu m$ (left) and $100\mu m$	2.4
10	(right) mean grain sizes	24
12	Effect of grain size on von Misses stress fields under force control for $5\mu m$ (left)	24
12	and $100\mu m$ (right) mean grain size.	24
13	Δ CMD, Δ CTD, and $\Delta\delta$ 5 for multiple microstructural gradients under displacement	26
14	control. Colors represent different microstructural realizations	20
14	Δ CMD, Δ CTD, and $\Delta\delta$ 5 for multiple microstructural gradients under force control. Colors represent different microstructural realizations.	27
15	Δ CMD, Δ CTD, and $\Delta\delta$ 5 for multiple microstructural Y-axis gradients under dis-	21
13	placement control. Colors represent different microstructural realizations	28
16	Δ CMD, Δ CTD, and $\Delta\delta$ 5 for multiple microstructural Y-axis gradients under force	20
10		29
17	control. Colors represent different microstructural realizations Δ CMD, Δ CTD, and $\Delta\delta$ 5 for multiple microstructural X-axis gradients under dis-	23
1.7	placement control. Colors represent different microstructural realizations	30
18	Δ CMD, Δ CTD, and $\Delta\delta$ 5 for multiple microstructural X-axis gradients under force	50
10	control. Colors represent different microstructural realizations	31
19	Δ CMD, Δ CTD, and $\Delta\delta$ 5 for two texture gradients under force control. Colors	31
1)	represent different microstructural realizations.	33
20	Δ CMD, Δ CTD, and $\Delta\delta$ 5 for X-axis gradients and mean grain size of $5\mu m$ under	55
20	force control. Colors represent different microstructural realizations	34
21	Δ CMD, Δ CTD, and $\Delta\delta$ 5 for Y-axis gradients under force control and two mean	5-1
_1	grain sizes. Colors represent different microstructural realizations	35
	Orani silbi. Corora represent anterent interest actual femilianism.	

22	Boxplots summarizing normalized distributions of maximum Δ CMD, Δ CTD, and $\Delta\delta$ 5 values for multiple texture gradients along X-axis and mean grain size of $5\mu m$	
	under force control	35
23	Boxplots summarizing normalized distributions of maximum Δ CMD, Δ CTD, and	
	$\Delta\delta 5$ values for multiple texture gradients along Y-axis under force control	36
24	Stress-strain curves for two Nickel single crystals and two polycrystals from dif-	
	ferent manufacturers. Solid lines correspond to simulations while symbols corre-	
	spond to experiments from the literature	39
25	Δ CMD, Δ CTD, and $\Delta\delta$ 5 for multiple equiaxed microstuctural realizations under	
	force control. Colors represent different microstructural realizations	40
26	Δ CMD, Δ CTD, and $\Delta\delta$ 5 for X-axis gradients and mean grain size of $2\mu m$ under	
	force control. Colors represent different microstructural realizations	41
27	Boxplots summarizing normalized distributions of maximum Δ CMD, Δ CTD, and	
	$\Delta\delta 5$ values for multiple texture gradients along X-axis under force control	42

1 Introduction

Fracture failure is an intrinsic multiscale problem: on the one hand, loads or displacements are applied far from the crack on a "macroscopic" scale. On the other hand, crack blunting, growth and failure depend on the atomic decohesion and defect aggregation (e.g., dislocations, vacancies), both of which are strongly sensitive to the local atomistic energetic state. Such a sensitivity controls what sometimes it is referred to as "crack tip mechanics". For instance, the environment may place a strong role on the energetic state of atoms, facilitating brittle or ductile failure. However, the environment does not usually affect the bulk of the material at the macroscopic scale.

Traditional fracture mechanics approaches such as Linear-Elastic or Elasto-Plastic Fracture Mechanics (LEFM or EPFM) are based on singularity models and rely on the assumption that stress and strain fields are self-similar [1]. The popularity and success in engineering applications of these theories rely on a key capability: the ability to infer the local crack growth driving force at the crack tip by surveying macroscopic physical magnitudes away from the crack tip. Thus, engineers employ nominal macroscopic forces or displacements in structures and components to estimate the potency for stable or unstable crack growth.

This remarkable ability to predict crack failure from macroscopic loading is based on solid theoretical grounds that connect singularity fields, energy release rate and fracture failure. Among the underlying assumptions is that materials are isotropic and homogeneous. If these requirements are not satisfied, traditional fracture approaches are not fully theoretically sound. For instance, metallic components manufactured by rolling, welding, or additive technology can introduce strong heterogeneity or anisotropy that are usually neglected in fracture models or taken into account with *ad-hoc* correction coefficients that carry a large uncertainty. Furthermore, these approaches are not amenable with physic-based and materials genome [2, 3] efforts that aim to predict and design material properties from first principles.

1.1 Fundamentals of fracture and microstructure relation

Most manufacturing routes introduce some heterogeneity in metallic materials that may affect crack growth. For example, Figure 1 exemplifies a crack growing towards an interface at which the material properties change abruptly—e.g., welded material and the heat affect zone. In such cases, the J-integral becomes path-dependent and shielding or amplification effects arise depending on the material properties on each size of the interface [4, 5, 6]. Certainly, the J-integral in the neighborhood of the crack tip (J_{tip}) may still represent crack growth driving force, but its value differs from the J-integral measured far from the crack (J_{far}) . In consequence, standardized measurements for K and J based on far field magnitudes (e.g., ASTM E1820 [7]) may not yield accurate predictions of the driving force that control fracture. Moreover, this inaccuracy applies both during the integrity assessment of a component or the measurement of materials fracture toughness critical values (e.g., K_{IC} and J_{IC}).

Heterogeneity and anisotropy observed in most engineering materials are not properly con-

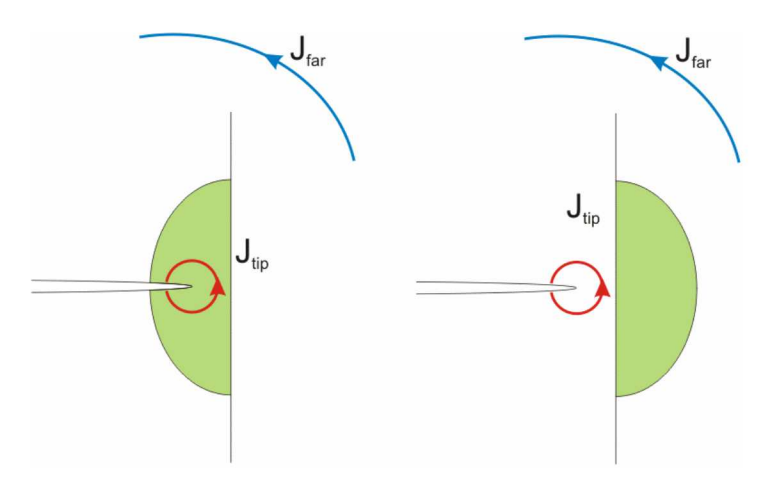


Figure 1: Crack-tip shielding or amplification of plastic zones that are indicated by the shaded areas. (a) crack-tip shielding $J_{tip} < J_{app}$ (b) crack-tip amplification $J_{tip} > J_{app}$.

sidered in traditional fracture mechanics approaches. Progress in understanding the role of microstructure on fracture requires an unequivocal definition of the driving force that does not depend on material properties. For instance, CTOD, K or J-integral can be estimated by measuring the crack mouth opening displacement or the work done on a specimen. However, these estimations depend on material properties and models that are ill-defined for heterogeneous material (e.g., grain size and composition gradients, crystallographic texture).

One strategy towards the disambiguation from ill-defined material properties is the use of driving forces that can be measured directly, such as energy, forces and displacements; indeed, these magnitudes are defined independently of the material. Thus, this research relies on comparing displacements to assess the fracture driving forces. We prefer displacements over energy and force because we can distinguish local (at the crack tip) from far field magnitudes, and we can easily differentiate opening and sliding modes. Furthermore, displacements maintain their physical meaning up to the atomistic scale and they can be correlated with crack blunting and growth by quantifying the number of Burger's vectors emitted from the crack tip.

The following sections analyze the local crack growth driving forces for multiple microstructural arrangements with identical "far field" conditions (i.e. force or displacement controlled boundaries). The fracture driving forces correspond to the crack mouth displacement (CMD) [7], the crack tip displacement (CTD) [7], or $\delta 5$ [8]. These magnitudes provide a simple and clear bases for comparing microstructural effects. In summary, the objective of this research is to assess the effects of microstructures such as grain sizes and crystallographic textures on displacement-based fracture driving forces.

2 Modeling approaches

This work assumes that crack tip mechanics are identical in all simulations, but changes are introduced on the mesoscale that mediates between the crack tip and the macroscale. The implications behind such an assumption is that the environment effect is null and the crack tip shape is initially identical for all cases. Since we do not aim to identify critical fracture toughness magnitudes (which we assume identical), we only require a constitutive model that conveys mesoscale variability. Furthermore, we assume that local fracture toughness is high enough to prevent crack growth. In other words, our objective is to understand the crack neighborhood that controls fracture ductile failure during crack blunting and before crack growth (stable or unstable).

Microstructure can be conveyed into models in myriads of ways, but only physics-based models can confidently extrapolate the mechanical response outside the experimental set used for validation; these models can then be employed to calibrate reduced order models. One of the main challenges of multiscale plasticity is the mesoscale heterogeneity and anisotropy. Both aspects must be accurately modeled to predict the local crack tip behavior. Indeed, the crack tip opening might span from a few atomic distances to hundreds of microns, and it is precisely in this mesoscale range in which microstructural effects are most noticeable.

The crystal plasticity formulations [9, 10] are the simplest continuum models that explicitly quantifiy the plastic anisotropy from the crystal orientation of individual grains (e.g., texture). These attributes are extremely difficult to describe with higher scale models such as isotropic J_2 plasticity theory, which does not track slip system activity or its crystallographic orientation dependence. Hence, we employ two local 3D crystal plasticity finite element models for FCC metals implemented as an Abaqus user subroutine (UMAT) [11]. Further information about the constitutive models is presented in sections 2.2 and 4.1.

2.1 Meshes and microstructures

This research studies "long cracks" with length over width ratio of a/w=0.5 and a semi-circular crack tip with about 16 elements as shown in Figure 2. The model has a one-element thickness without any out-of-plane constraint, which represents a plane stress condition. Such a geometry is typical of elasto-plastic fracture mechanics models except for the limited crack tip mesh refinement, which is imposed to reduce the computational burden of the crystal plasticity model. To mitigate the impact of such coarse mesh, we consider driving forces that avoid measuring internal state variables at the maximum strained elements. Instead, we estimate the fracture driving force based on the displacements measured at the crack mouth (CMD), tip (CTD) and ahead the crack (δ 5), see Figure 2. These are fundamental magnitudes that can be measured directly without any assumption; on the contrary, the estimation of driving forces such as K or J are indirect measurements that can be strongly sensitive to mesh sizes, geometry and material properties.

Loading consisted of the quasi-static force or displacement increments to the right side of the mesh along the X-axis (Figure 2), while the left side is constrained along the X direction. Upon

reaching the maximum load, the opening and sliding components of the CTD, CMD, and $\delta 5$ are computed. Under displacement control, nominal deformations up to 2% and 5% are applied for the models in sections 2.2 and 4.1, respectively. Under force control, the maximum load was estimated to yield approximately similar crack tip openings for the model with larger grain size. Furthermore, section 2.2 considers a strain rate of 10^{-2} s⁻¹ while section 4.1 uses 10^{-5} s⁻¹.

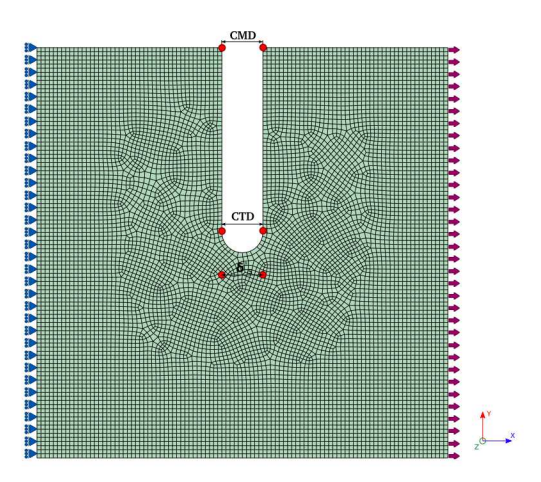


Figure 2: Finite element mesh in which the boundary conditions represented. The nodes considered for quantifying the crack tip driving forces CTD, CMD, and $\delta 5$ are highlighted.

Figure 3 presents examples of the microstructures employed thoughout the report. Here, we used six microstructures: (1) equiaxed fine grains (1000 grains), (2) equiaxed coarse grains (600 grains), (3) radially decreasing grain sizes, (4) radially increasing grain sizes, (5) decreasing grain sizes in +X direction and (6) decreasing grain sizes in +Y direction. For each grain we computed a grain diameter based on the total volume of an equivalent spherical grain. Such a grain size is used by the constitutive model. In addition, Figure 4 exemplifies the gradients in the crystallographic texture along X and Y direction (see the axis definition Figure 2). These microstructures consider a linear gradient from a perfect single crystal on one edge up to random orientation starting at the crack level.

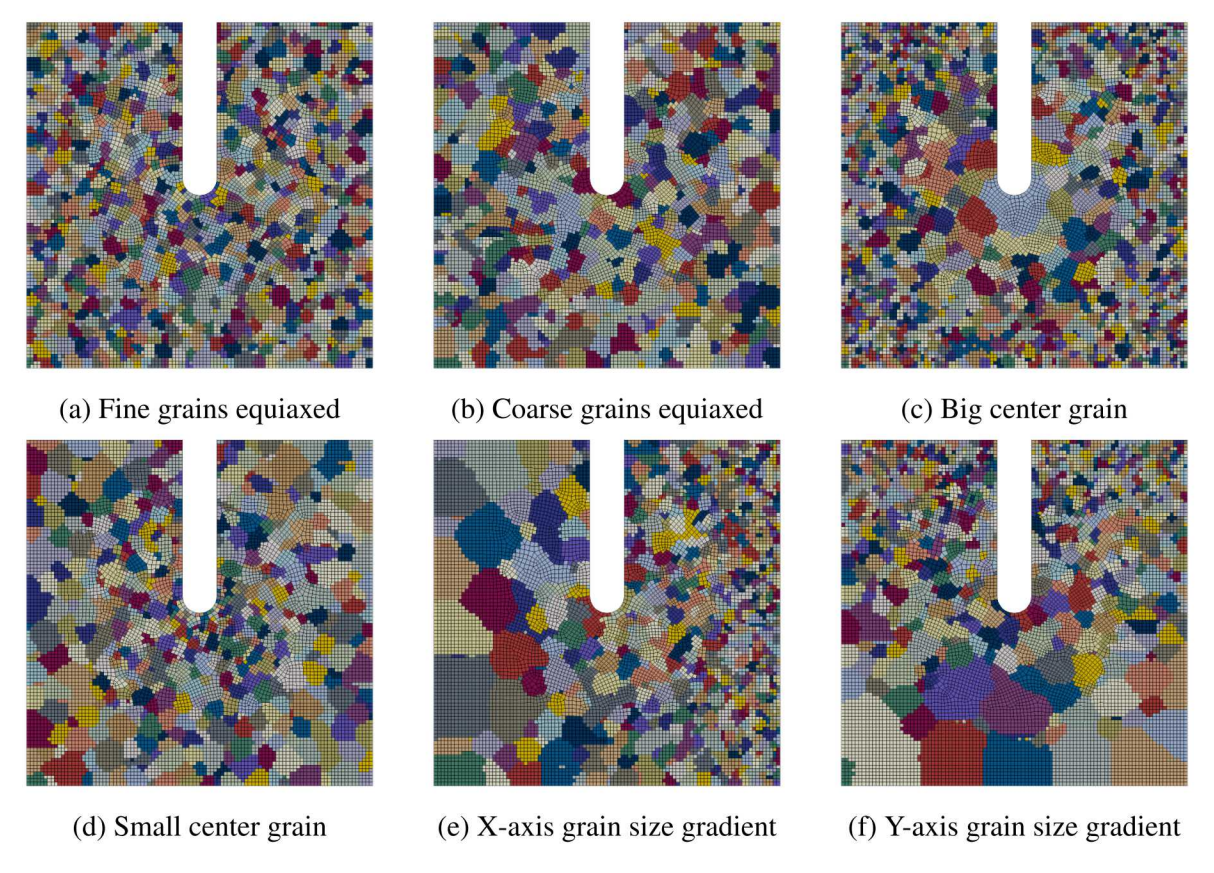


Figure 3: Multiple microstructures employed in the assessment of the crack tip driving force.

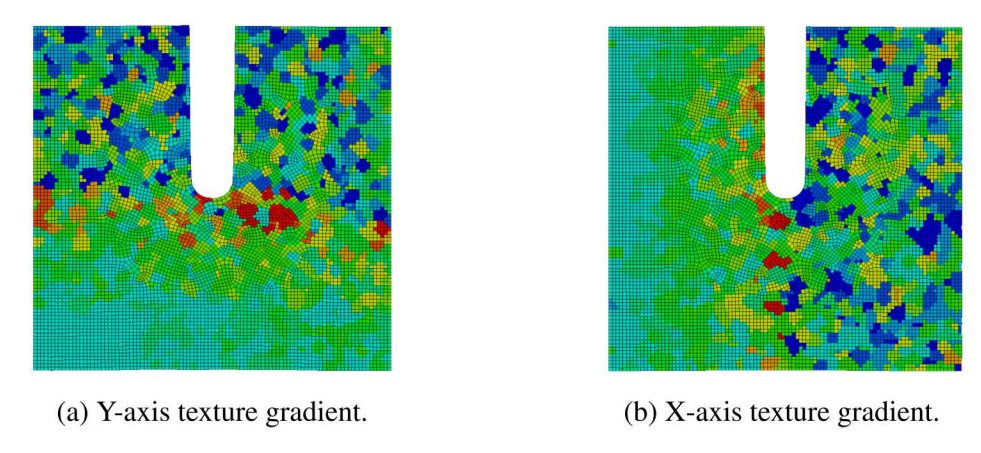


Figure 4: Texture gradients a long different axis. Colors refer schematically to the linear varitaion of the three Euler angle orientations.

2.2 Constitutive Model

Constitutive models have traditionally attempted to match experimental behavior by introducing ad-hoc mathematical formulations that depend on parameters and material constants. Over the last decades a new philosophy has arisen trying to enrich constitutive models with physical information with the hope to increase the predictive capability of models outside the range of macroscopic experimental data.

The goal is to propose physical models for each dominant deformation mechanisms, and the range of variability of these parameters are determined from experimental or modeling uncertainties independently from the macroscopic response. The bounds of parameters increase the confidence on the proposed mechanisms and serve as a critical tool to discard models that do not match the expected macroscopic response. This approach is much more than a mere sensitivity analysis, it is a modeling philosophy that pursues validation at multiple scales.

This research adapted rate dependent crystal plasticity model for pure Nickel from a prior research program [12]; this material is usually regarded as a proxy for Austenitic stainless steel. The model conveys the physics of dislocation interactions at multiple length scales. At the atomistic scale, shear strain depends on thermally activated dislocation glide while stress follows dislocation-dislocation interactions. At the mesoscale, the localization of dislocations substructures induces internal stresses that increases hardening.

The behavior of dislocation structures are considered assuming two scenarios: Section 3 considers elastic dislocation walls, which was the focus of prior research. Secondly, Section 4 improves the fidelity of the model by considering plastically deformable dislocation walls. In this case, we compare the results to single- and polycrystalline experimental results from the literature.

3 Elastic dislocation walls

Upon plastic deformation, evolution of dislocations tends to control the mechanical responses of metallic materials. In most metals, and particularly in FCC metals, dislocations tend to localize and form regions of low and high dislocation densities. The regions, usually referred to as low energy dislocation structures (LEDS) [13, 14], have been observed by TEM microscopy and are known to influence the mechanical responses. These structures are significantly stiffer than the materials in between and impose a constraint to plastic deformation. In the cases of cyclic loading, these structures are responsible for the development of a back stress.

Prior work has developed a constitutive model that explicitly incorporate the influence of elastic dislocation walls. This model assumes that screw dislocations develop in between the walls, which constraint the mean free path of dislocations and the local stresses as described in the following section.

3.1 Constitutive Formulation

The constitutive model is implemented in Abaqus using a physics-based philosophy that avoids fitting coefficients without clear physical meaning. Instead, all parameters can be estimated from lower length scale measurements or modeling, and the only "fitting" flexibility is within the uncertainty of the parameters. Clearly, this approach is perfectly positioned for uncertainty quantification.

The shear rate of the α -th slip system follows the Arrhenius thermal activation proposed by Kocks et at. [15, 16],

$$\dot{\gamma}^{\alpha} = \rho_m^{\alpha} l_{struct} b v_G \exp\left(-\frac{F_0}{k_b T} \left(1 - \left[\frac{\left\langle \left|\tau_{eff}^{\alpha}\right| - S_0^{\alpha}\right\rangle}{s_t^0 \frac{C_{44}}{c_{44}^0}}\right]^p\right)^q\right) \operatorname{sgn}\left(\tau_{eff}^{\alpha}\right),\tag{1}$$

in which:

 ρ_m^{α} : Dislocation density for slip system, α

*l*_{struct}: Mean dislocation path,

b: Burgers vector,

 v_G : Lattice vibration frequency,

 F_0 : Activation energy for dislocation motion when the effective shear stress is zero,

 s_t^0 : Thermal slip resistance at 0K,

p, q: Profile parameters,

T: Temperature,

 k_b : Boltzmann constant.

 C_{44} : Elastic constant temperature T,

 C_{44}^0 : Elastic constant at 0K.

The athermal or threshold stress (S_0^{α}) depends on three contributions:

$$S^{\alpha} = S_0^{\alpha} + \alpha_{LE} \frac{\mu b}{d_{struct}} + \mu b \left(A_{\alpha\alpha} \rho_m^{\alpha} \right)^{1/2}$$
 (2)

The first term corresponds to the lattice thermal friction (S_0^{α}) , which becomes almost negligible in FCC metals compared to the contributions from dislocation interactions. The second term corresponds to the bow-out stress, and assumes irreversible deformation will not occur before a bow-out reaches a critical length (d_{struct}) . This term depends on the dislocation line energy factor (α_{LE}) . The third term corresponds to the dislocation-dislocation interaction strength for dislocations on the same slip system and depends on parameter $A_{\alpha\alpha}$, which is usually about $\sqrt{A_{\alpha\alpha}} = 0.35$.

The mean dislocation path and the typical dislocation size are assumed to be identical and follow similared with $K \sim 8 - 10 \mu m$ [17]:

$$d_{struct} = l_{struct} = \frac{K\mu b}{\tau^{\alpha}},\tag{3}$$

where, μ is Hill's shear modulus. The dislocation density is computed following the balance rate:

$$\dot{\rho}_{m}^{\alpha} = \left[\frac{1}{bl_{struct}} - \frac{2y_{s}}{b} \rho_{m}^{\alpha} \right] |\dot{\gamma}^{\alpha}| + \frac{d_{struct}}{d_{0}t_{0}} \left(\phi_{cs} \rho_{m}^{\zeta} e^{-V_{cs} \frac{\tau_{III} - \tau^{\alpha}}{k_{B}T}} - \rho_{m}^{\alpha} e^{-V_{cs} \frac{\tau_{III} - \tau^{\zeta}}{k_{B}T}} \right)$$
(4)

This first term corresponds to dislocation multiplication and annihilation, while the second term corresponds to the probability of cross slip of mobile dislocations from plane α to ζ . Here,

 y_s : Annihilation distance for edge dislocations,

 d_0, t_0 : Cross slip reference distance and time,

 ϕ_{cs} : Cross slip efficiency,

 V_{cs} : Cross slip volume,

 τ_{III} : Cross slip stress.

Cross slip volume and stress are computed as follows:

$$V_{cs} = \frac{V_{cs}^0}{\tau^\alpha - B^\alpha} \tag{5}$$

$$\tau_{III} = \frac{\mu b}{4\pi v_{\rm s}} \tag{6}$$

The effective stress (τ_{eff}^{α}) is defined as the macroscopic shear stress less the internal stress (B^{α}) as follows:

$$\tau_{eff}^{\alpha} = \tau^{\alpha} - B^{\alpha} \tag{7}$$

The internal or back stress is computed from:

$$\dot{B}^{\alpha} = \frac{f_w}{1 - f_w} \frac{2\mu \left(1 - 2S_{1212}\right)}{\left(1 + 4\mu S_{1212} f_{Hill}\right)} \gamma^{\alpha} \tag{8}$$

in which f_w is the dislocation wall fraction, f_{Hill} is the accommodation factor and S_{ijkl} is the Eshelby tensor for a prolate spheroid. These are computed as:

$$fw = f_{inf} + \left(f_0 - f_{inf}\right) \exp\left(\frac{-\gamma_p}{g_p}\right) \tag{9}$$

$$f_{Hill} = (1 - f_w) \left(1 - \frac{d_{struct}}{d_{gr}} \right) \frac{d\gamma^{\alpha}}{d\tau^{\alpha}}$$
 (10)

$$S_{1212} = \frac{\pi \eta_{struc}^2 + (\eta_{struc}^2 - 1.75 - 2v_p \eta_{struc}^2 + 2v_p) C_{I2}}{8\pi (1 - v_p) (\eta_{struc}^2 - 1)}$$
(11)

$$C_{I2} = \frac{2\pi \eta_{struc} \left(\eta_{struc} \sqrt{\left(\eta_{struc}^2 - 1 \right) - \cosh^{-1} \left(\eta_{struc} \right) \right)}}{\sqrt{\left(\eta_{struc}^2 - 1 \right)^3}}$$
(12)

$$\mu_p = \frac{\mu}{1 + 2\mu \, f_{Hill}} \tag{13}$$

$$v_p = \frac{v + \frac{2}{3}\mu (1 + v) f_{Hill}}{1 + \frac{4}{3}\mu (1 + v) f_{Hill}}$$
(14)

Note that this equation conveys a grain size dependence through the accommodation factor.

3.2 Material parameters and physical constants

Constitutive models depend on three types of parameters: Direct, stochastic and initial parameters. Direct parameters correspond to physical constants that are intrinsic to the material and do not correspond to the mesoscopic response of a statistical ensemble. These parameters are deduced from experimental measurements or first principle calculations and are linked to fundamental physics. For instance:

Boltzmann constant, k_b ,

Temperature, T = 300K,

Atomic jump frequency, $v \sim 10^{12} s^{-1}$,

Burger's vector, $b = 2.5 \times 10^{-10}$.

The elastic constants are also considered a fundamental quantity that can be computed from the first principles (even though they are the result of a quantum statistical ensemble). Here we employ: $C_{11} = 249GPa$, $C_{12} = 155GPa$, $C_{44} = 114GPa$, $C_{44}(0K) = 128GPa$ and shear modulus $\mu = 80.6GPa$,

Stochastic parameters are associated with mechanisms or theoretical models that describe the behavior of a statistical ensemble. Among these quantities are energy barrier parameters, dislocation interaction strengths, the cross slip activation energy and volume, etc. These quantities can be estimated by indirect experimental measurements or by simulations such as dislocation dynamics, and they are characterized by a much larger intrinsic uncertainty than direct parameters. The stochastic parameters employed here are,

Activation energy, Fo = 0.93 eV,

Thermal slip resistance at 0K, $s_t^0 = 90MPa$,

Profile parameters, p = 1, q = 1.5.

Annihilation distance for edge dislocations (not induced by cross slip) $y_s = 2nm$,

Intrinsic lattice friction, $S_0^{\alpha} = 4MPa$,

Dislocation-dislocation self interaction, $A_{ii} = 0.122$,

Line tension coefficient, $\alpha_{LE} = 0.5$,

Cross slip activation volume constant, $V_C^0 S = 20000b^3$,

Cross slip efficiency, $\phi_{CS} = 0.5$.

And the initial parameters are the initial density of mobile dislocations, $\rho_{m0}^s = 10^{10} m^{-2}$, and the initial structural distance $\sim 10 \mu m$.

3.3 Smooth specimen results

The macroscopic responses of polycrystal spencimens for different mean grain sizes are reproduced in Figure 5. These responses were computed by modeling the smooth bar shown in Figure 5a under quasi-static displacement-control deformation along the X-axis.

These figures present two major characteristics: a reduction in grain size increases the stress and grain size effects saturate for dimensions about $500\mu m$. This constitutive response will be employed in what follows to assess the fracture toughness driving forces. Section 4 will revisit constitutive behavior with models that match single- and poly-crystal experiments.

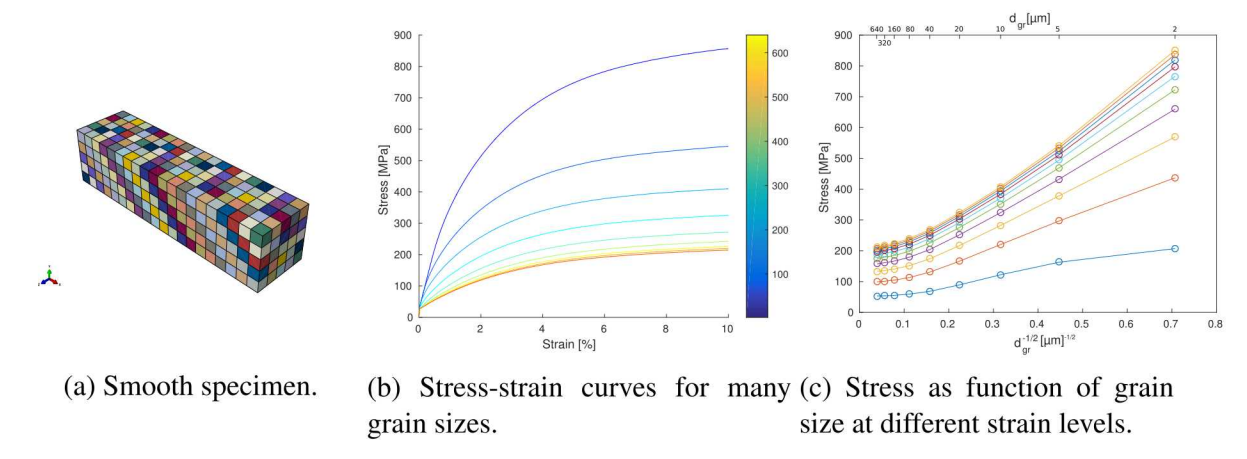


Figure 5: Constitutive responses of smooth specimens assuming elastic dislocation structures.

3.4 Results for equiaxed fine microstructures

Here we present the results of multiple microstructural realizations using equiaxed fine grains (Figure 3a) under displacement and force control. All simulations are equivalent except for the location and orientation of grains, i.e. multiple microstructural realizations were created with the similar number of grains and random crystal orientations were assigned. The results from multiple simulations are presented as the evolution over time of changes of CMD, CTD and $\delta 5$ (i.e., ΔCMD , ΔCTD , and $\Delta \delta 5$).

Results for displacement control

Figure 6 presents the evolution of the opening (left) and sliding (right) components of the Δ CMD, Δ CTD, and $\Delta\delta$ 5 for five microstructural realizations under displacement control. For each microstructural realization we modeled either $5\mu m$ or $100\mu m$ mean grain sizes. In addition, we consider an homogeneous J2 plasticity model constructed with the piece-wise stress-strain curve in Figure 5b.

These results suggests that under displacement control, the change in CMOD is almost insensitive to grain size effects. On the contrary, the microstructure induces non-negligible sliding components, and they may be positive or negative, which means that shear could occur in both directions. Interestingly, the homogeneous case has no shear component, which suggest that microstructure induce some Mode II deformation which is not predicted unless the microstructure is considered.

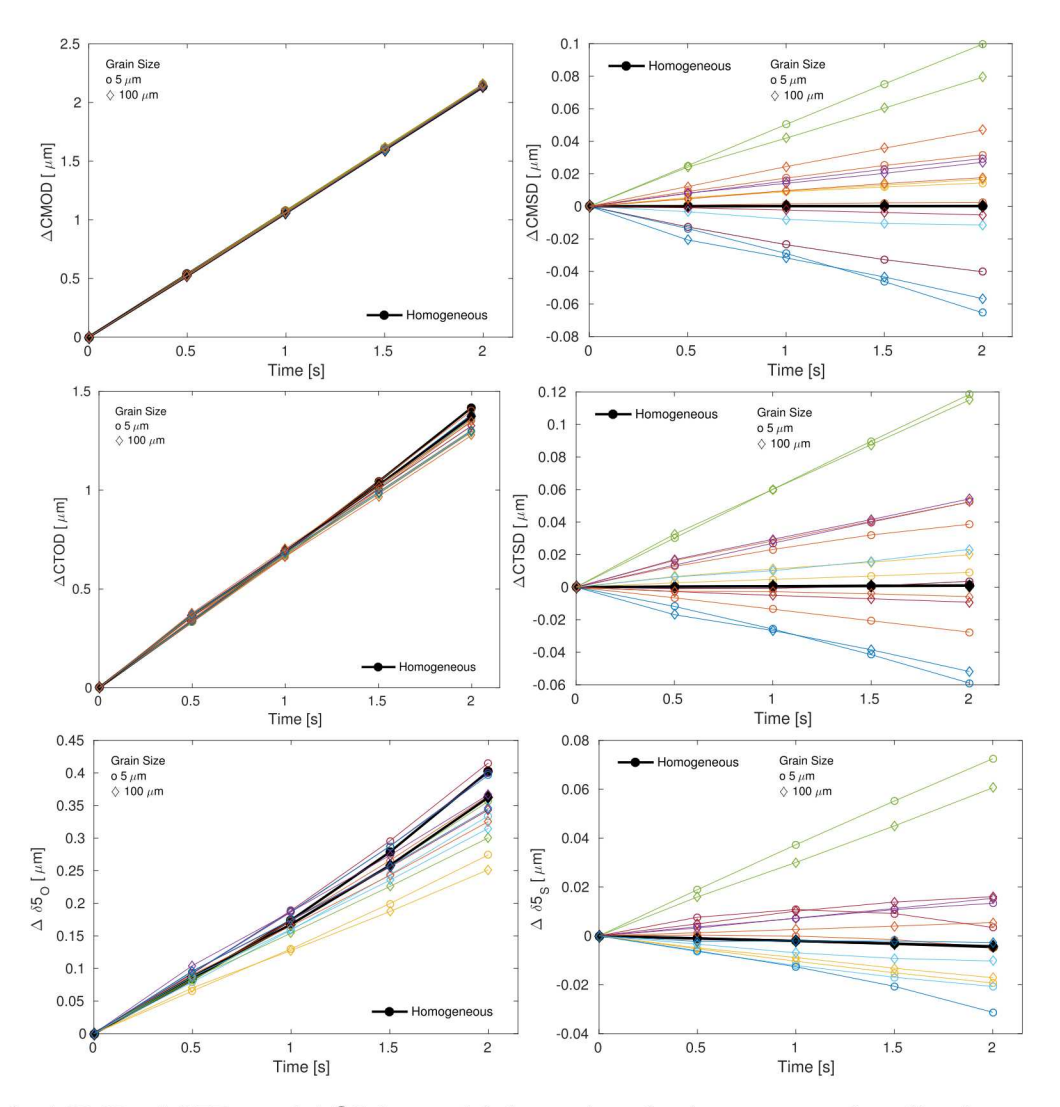


Figure 6: Δ CMD, Δ CTD, and $\Delta\delta$ 5 for multiple equiaxed microstructural realizations under displacement control. Colors represent different microstructural realizations. Black correspond to homogeneous J2 model.

Force control

Figure 7 presents the evolution of the opening (left) and sliding (right) components of the Δ CMD, Δ CTD under force control. We consider ten microstructural realizations with $5\mu m$ or $100\mu m$ mean grain sizes and a homogeneous J2 model as previously described. The total force was selected such that the CTD of the largest grain size is approximately the same as in the case of displacement control.

Contrary to the findings under displacement control, the grain size has a great impact on the opening and sliding displacements. Even within the same grain size, the variability increases significantly and the homogenized J2 model may not be representative of the mean behavior. The sliding components can again be positive or negative, but they are not negligible as in the case of

the homogeneous model.

The increase in variability and the impact of grain size effect suggest that force-control may induce higher uncertainty for distance-based fracture driving forces. Thus, though-out of the rest of the report puts more emphasis on the force-control scenario.

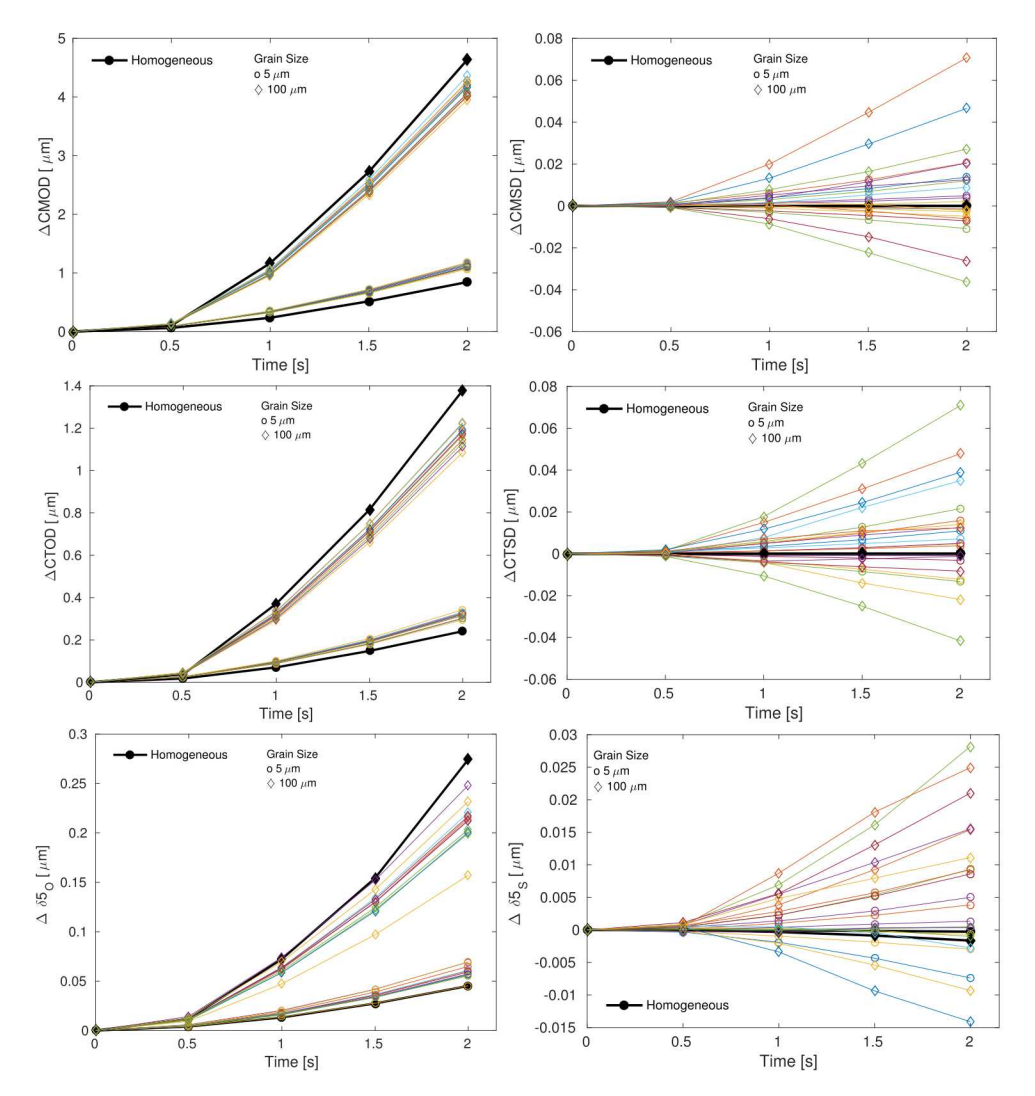


Figure 7: Δ CMD, Δ CTD, and $\Delta\delta$ 5 for multiple equiaxed microstructural realizations under force control. Colors represent different microstructural realizations. Black correspond to homogeneous J2 model.

Figure 8 summarizes in three box plots the normalized distributions of maximum Δ CMD, Δ CTD, and $\Delta\delta$ 5 values for multiple equiaxed microstructural realizations under force control; two grain sizes are also shown. The normalization factor correspond to the mean opening magnitude. The results show some clear trends:

• The variability of $\Delta \delta 5$ is higher than that for ΔCTD , which is still higher than that for ΔCMD . Thus, the closer we measure the displacement from the crack tip, the larger variability.

• The dispersion of Δ CMSD is much smaller than that from Δ CMOD. On the contrary, the spread of sliding and opening components of $\Delta\delta$ 5 are about the same. Such a difference suggests that far field measurements of the fracture driving force smears out Mode II component compared to Mode I.

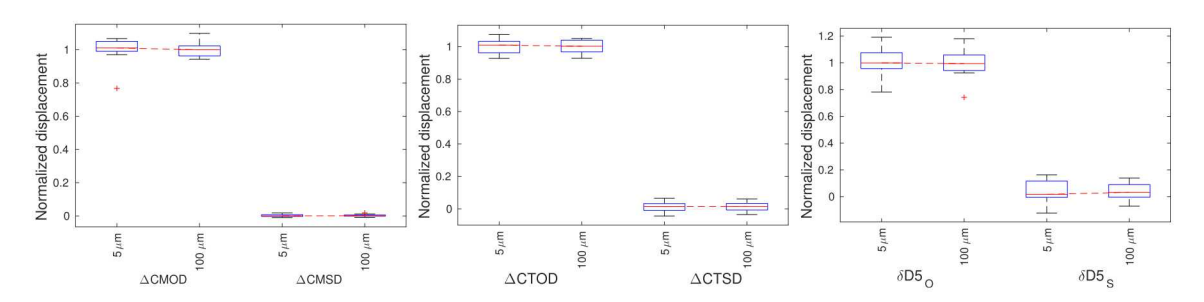


Figure 8: Boxplots summarizing normalized distributions of maximum Δ CMD, Δ CTD, and $\Delta\delta$ 5 values for multiple equiaxed microstructural realizations under force control.

3.5 Effects on stress and strain fields

In order to further compare the loading conditions we present the stress and strain fields for one realization with $5\mu m$ and $100\mu m$ mean grain sizes. The morphology of grains is the same in all cases.

Displacement control

Figures 9 and 10 depict the total strain and von Mises stress fields at maximum displacement, respectively under displacement control. Strain fields are almost identical in shape and peak magnitude, which correlates with the lack of sensitivity of driving forces to grain size effects. On the other hand, distributions of von Mises stress fields are similar for both grain sizes, but they scales differ significantly by a factor of two.

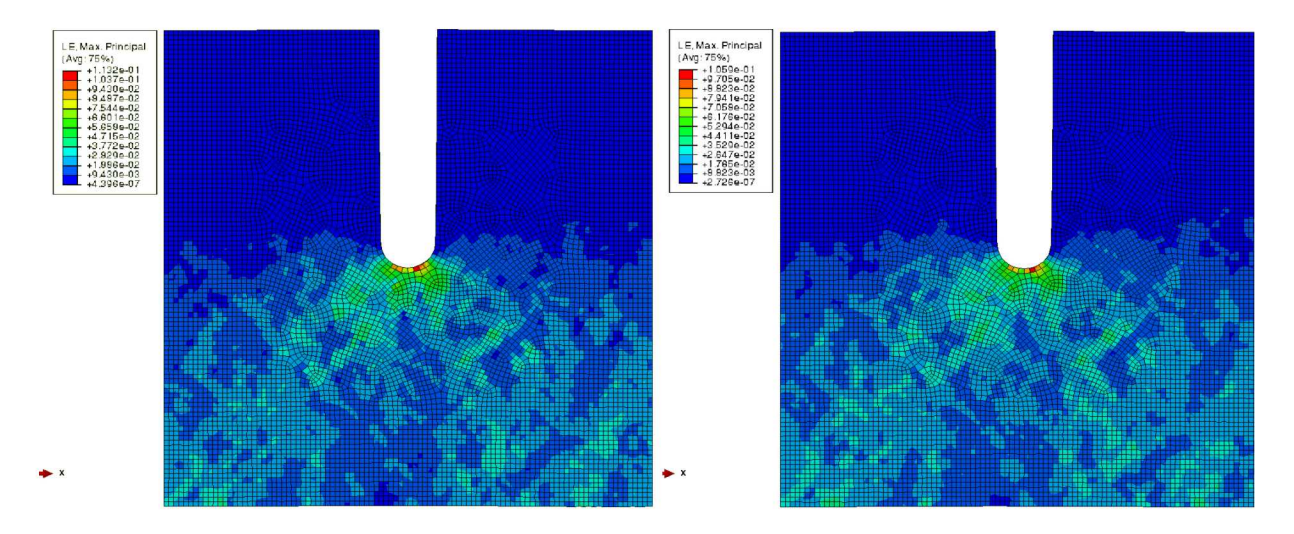


Figure 9: Effect of grain size on strain fields under displacement control for $5\mu m$ (left) and $100\mu m$ (right) mean grain sizes.

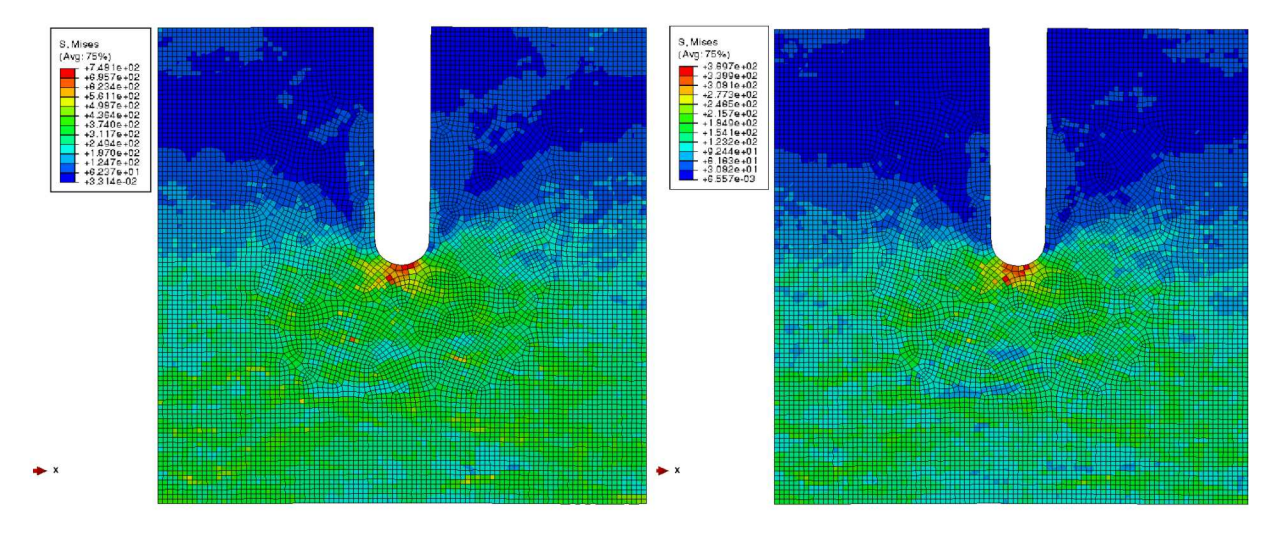


Figure 10: Effect of grain size on von Misses stress fields under displacement control for $5\mu m$ (left) and $100\mu m$ (right) mean grain sizes.

Force control

Figures 11 and 12 depict the total strain and von Mises stress fields at maximum force, respectively in force controlled simulations. In this case, as expected, von Mises stress field are almost identical in shape and peak magnitude in both cases. On the contrary, total strain fields are different and peak magnitudes differ by a factor of 3. Comparing with the last section, strain fields under force control seem more sensible to grain size than von Mises stress field under displacement control. Further research may clarify further these characteristics in order to minimize uncertainty.

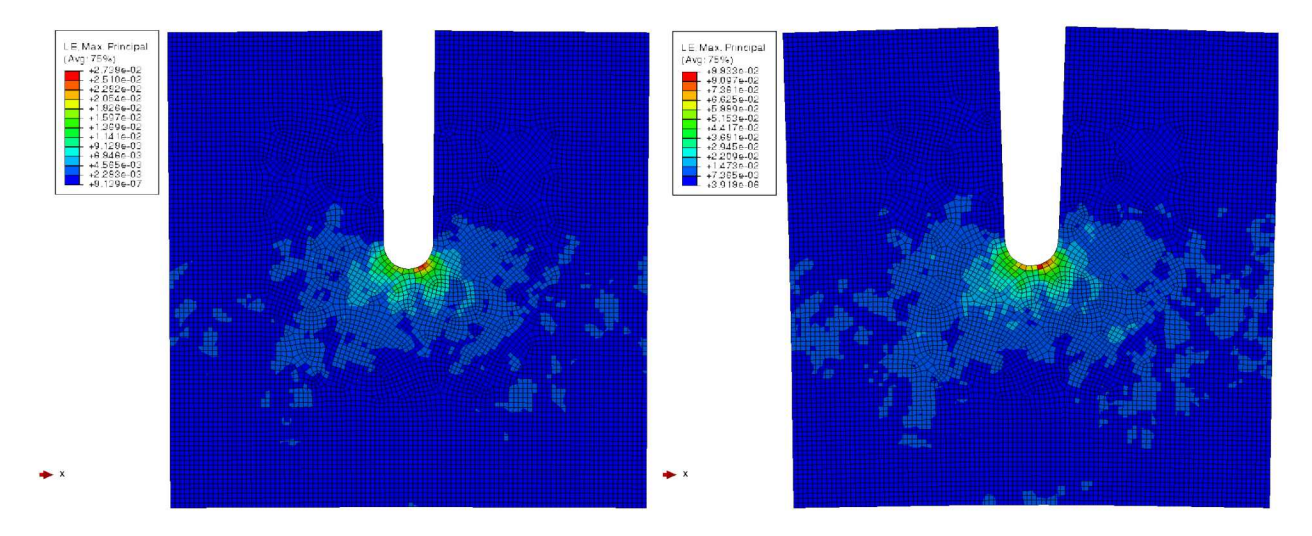


Figure 11: Effect of grain size on strain fields under force control for $5\mu m$ (left) and $100\mu m$ (right) mean grain sizes.

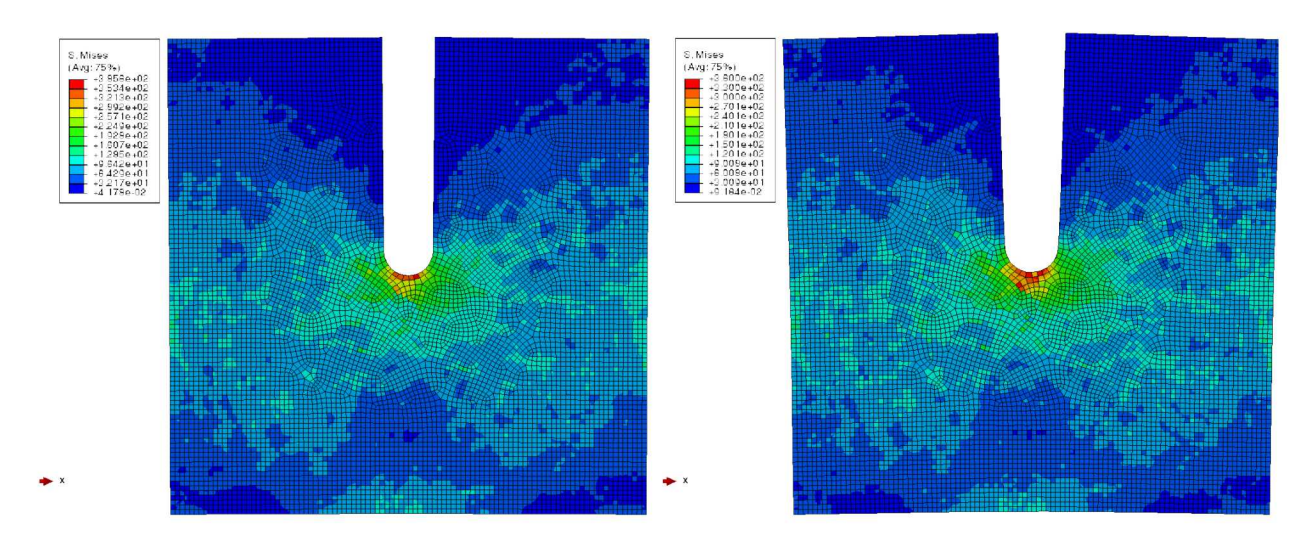


Figure 12: Effect of grain size on von Misses stress fields under force control for $5\mu m$ (left) and $100\mu m$ (right) mean grain size.

3.6 Results for microstructural gradients

As shown by simulations with equiaxed grains, microstructural variability propagates to fracture driving forces in various manners. This section explores the effect of different microstructural arrangements on a fracture driving force using various microstructures as shown in Figure 3. First, we review one realization per microstructure and later we assess five realizations for Y-axis and X-axis gradients.

Comparison among different microstructural gradients

Figure 13 presents the evolution of the opening and sliding displacements for microstructures with gradients under displacement control. Compared to the results for isotropic microstructures in Figure 6, microstructural gradients seem to increases the variability of all fracture driving forces. For instance, the Δ CTOD varies about 30% regardless of the grain size. Furthermore, the driving forces with identical microstructures but different mean grain size are correlated; this is particularly evident for the shear components, which tend to have the same sign for both grain sizes.

Figure 14 presents the evolution of the opening and sliding displacements for microstructures with gradients under force control. Similar to prior case, microstructural gradients seem to increase the variability of all fracture driving forces. Each grain size shows different mean values and both cases spread between 30% to 50%, but a rigorous quantification requires statistically meaningful number of realizations. In addition, the driving forces with identical microstructures and different mean grain size are strongly correlated. For instance, the same microstructure has the highest ΔCMD or $\Delta \delta 5$ for both mean grain sizes.

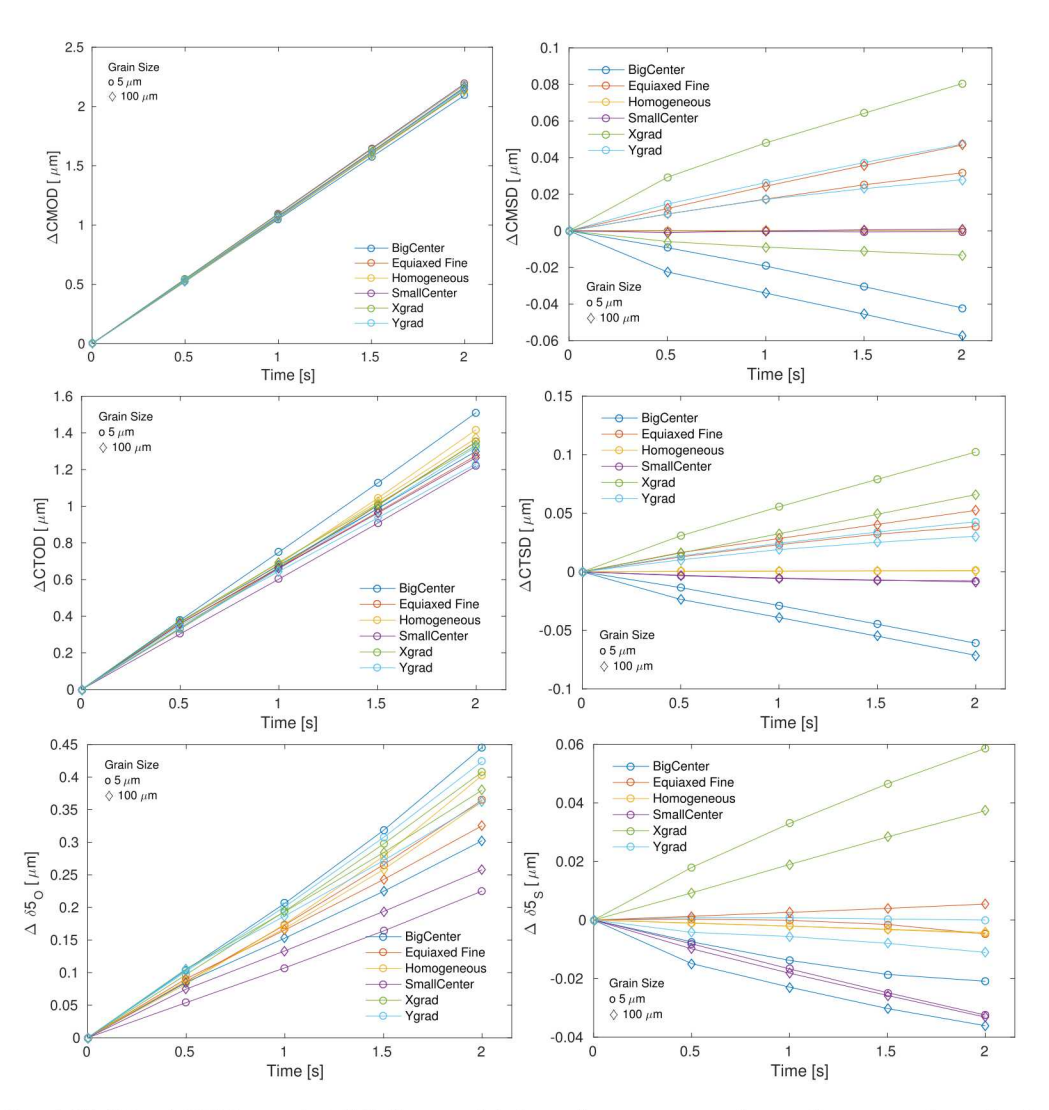


Figure 13: Δ CMD, Δ CTD, and $\Delta\delta$ 5 for multiple microstructural gradients under displacement control. Colors represent different microstructural realizations.

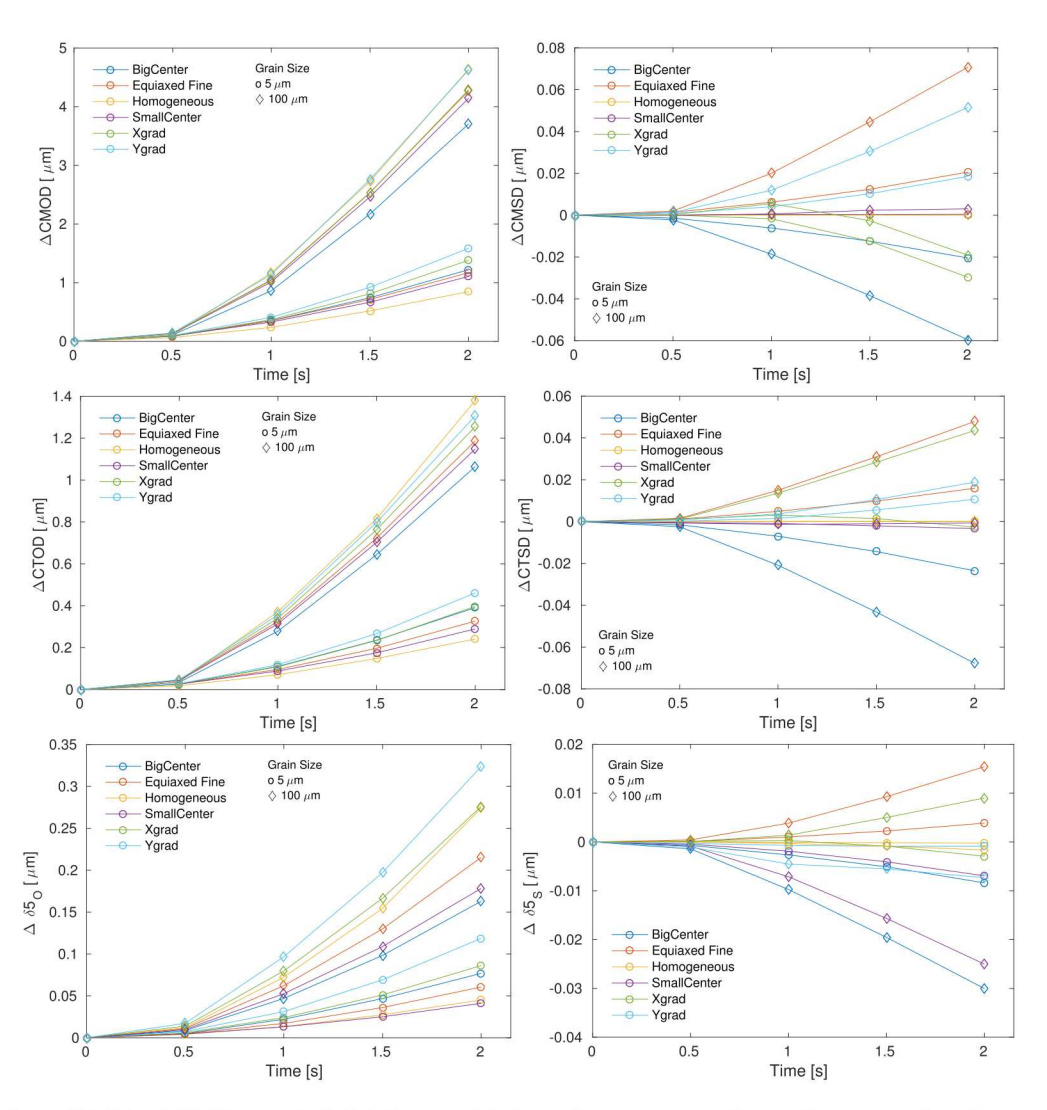


Figure 14: Δ CMD, Δ CTD, and $\Delta\delta$ 5 for multiple microstructural gradients under force control. Colors represent different microstructural realizations.

Y-gradients microstructural realizations

The previous section showed that microstructural gradients have a significant impact on driving forces, but more microstructural realizations are required to make strong conclusions. Thus, Figure 15 presents the evolution of the opening and sliding displacements for microstructures with gradients along the Y-axis under displacement control. These results are comparable to equiaxed isotropic microstructures from Figure 6 in terms of mean values and dispersion.

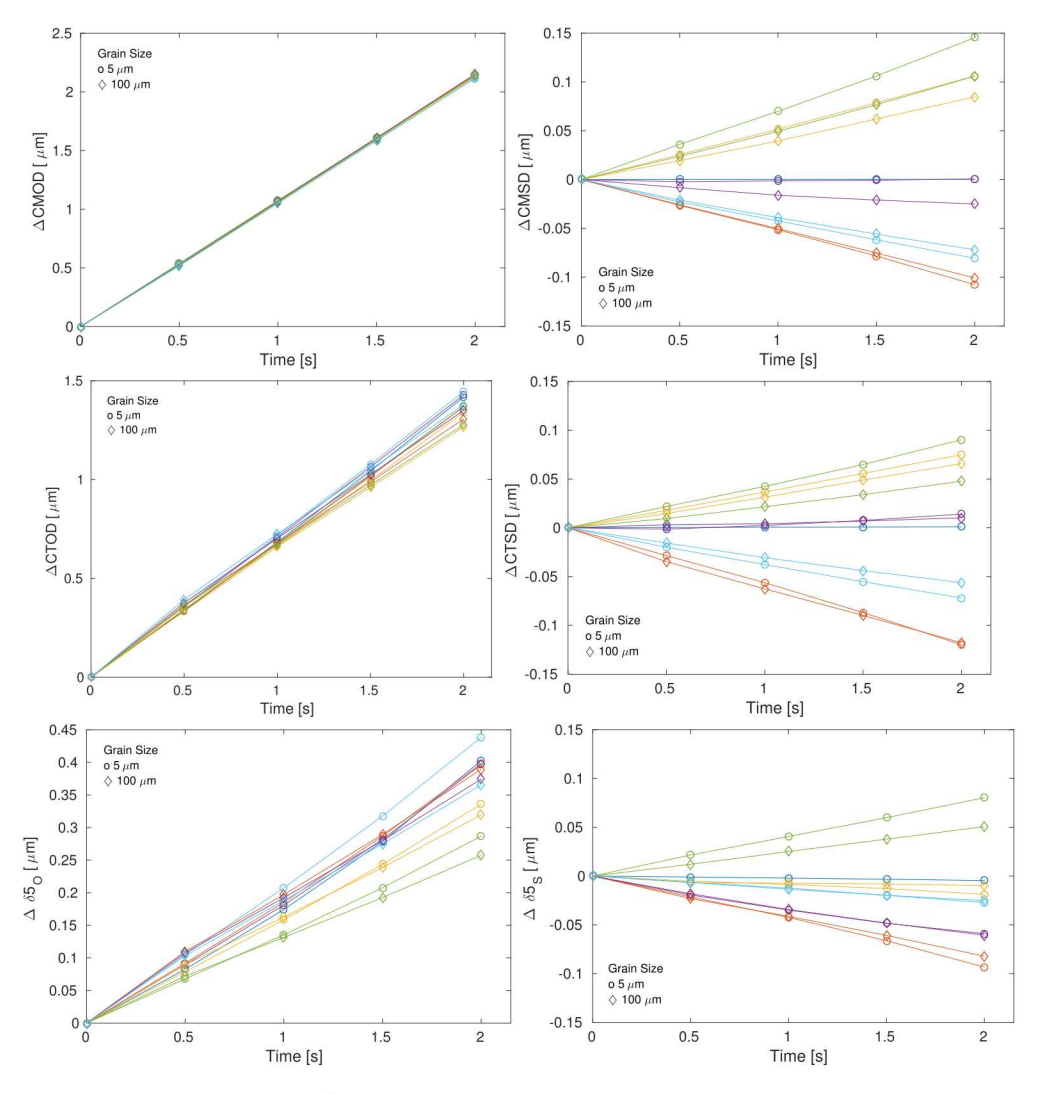


Figure 15: Δ CMD, Δ CTD, and $\Delta\delta$ 5 for multiple microstructural Y-axis gradients under displacement control. Colors represent different microstructural realizations.

Figure 16 presents the evolution of the opening and sliding displacements for microstructures with gradients along the Y-axis and force control. These results are comparable to equiaxed isotropic microstructures from Figure 7 in terms of dispersion, but the mean values seem slightly different. Although further statistics are required, opening displacements seem slightly higher than in the case of equiaxed microstructures while shear displacements seem to be asymmetric respect

to zero.

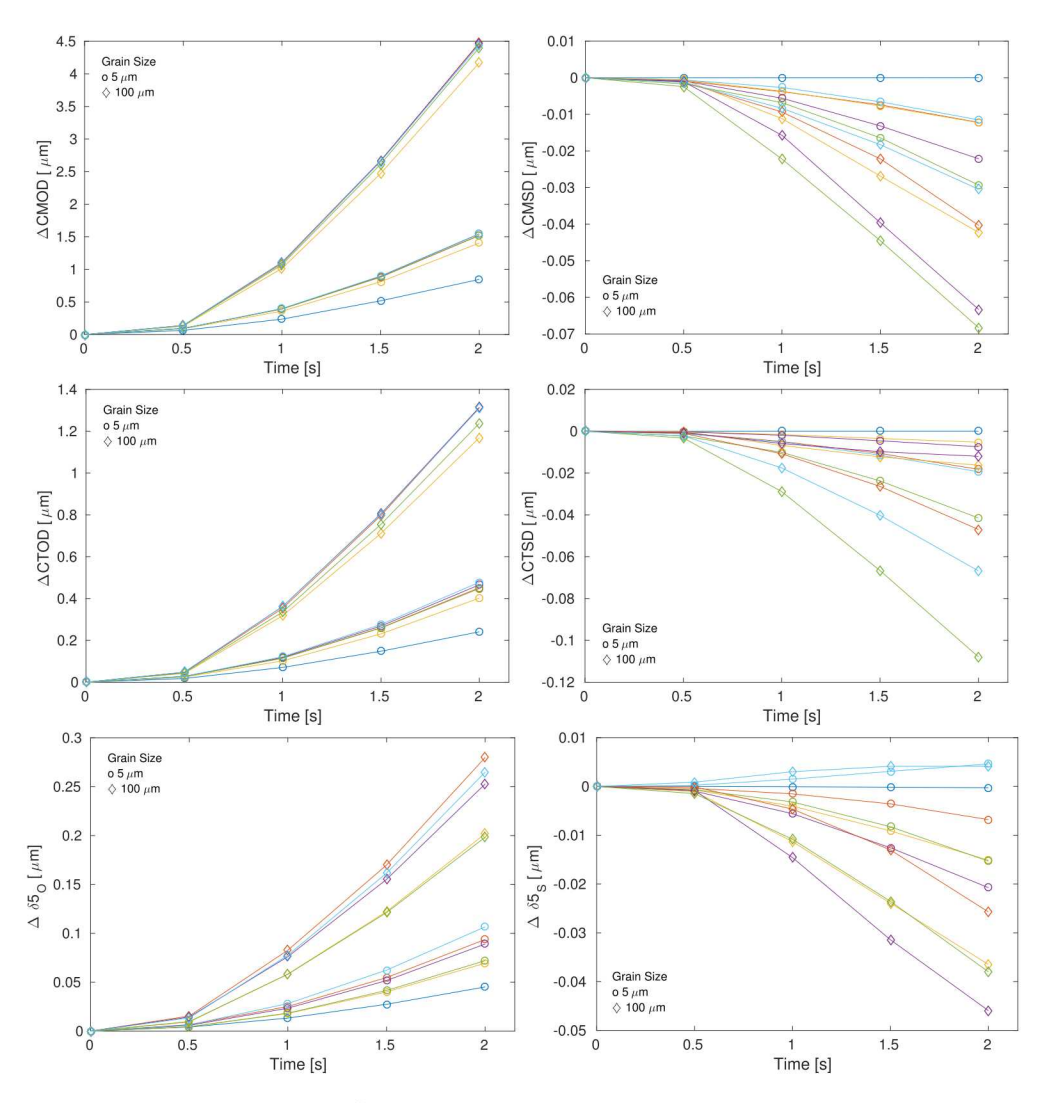


Figure 16: Δ CMD, Δ CTD, and $\Delta\delta$ 5 for multiple microstructural Y-axis gradients under force control. Colors represent different microstructural realizations.

X-gradients microstructural realizations

Figure 17 presents the evolution of the opening and sliding displacements for microstructures with gradients. Compared to Figure 6 and Figure 15, microstructural gradients along the X-axis has a greater effect on the Δ CMD variability. On the contrary, the $\Delta\delta$ 5 has a lower mean value and variability.

Figure 18 presents the evolution of the opening and sliding displacements for microstructures with X-axis gradients under force control. Compared to Figure 7 and Figure 16, microstructural gradients along the X-axis seem to induce larger Mode II towards one direction.

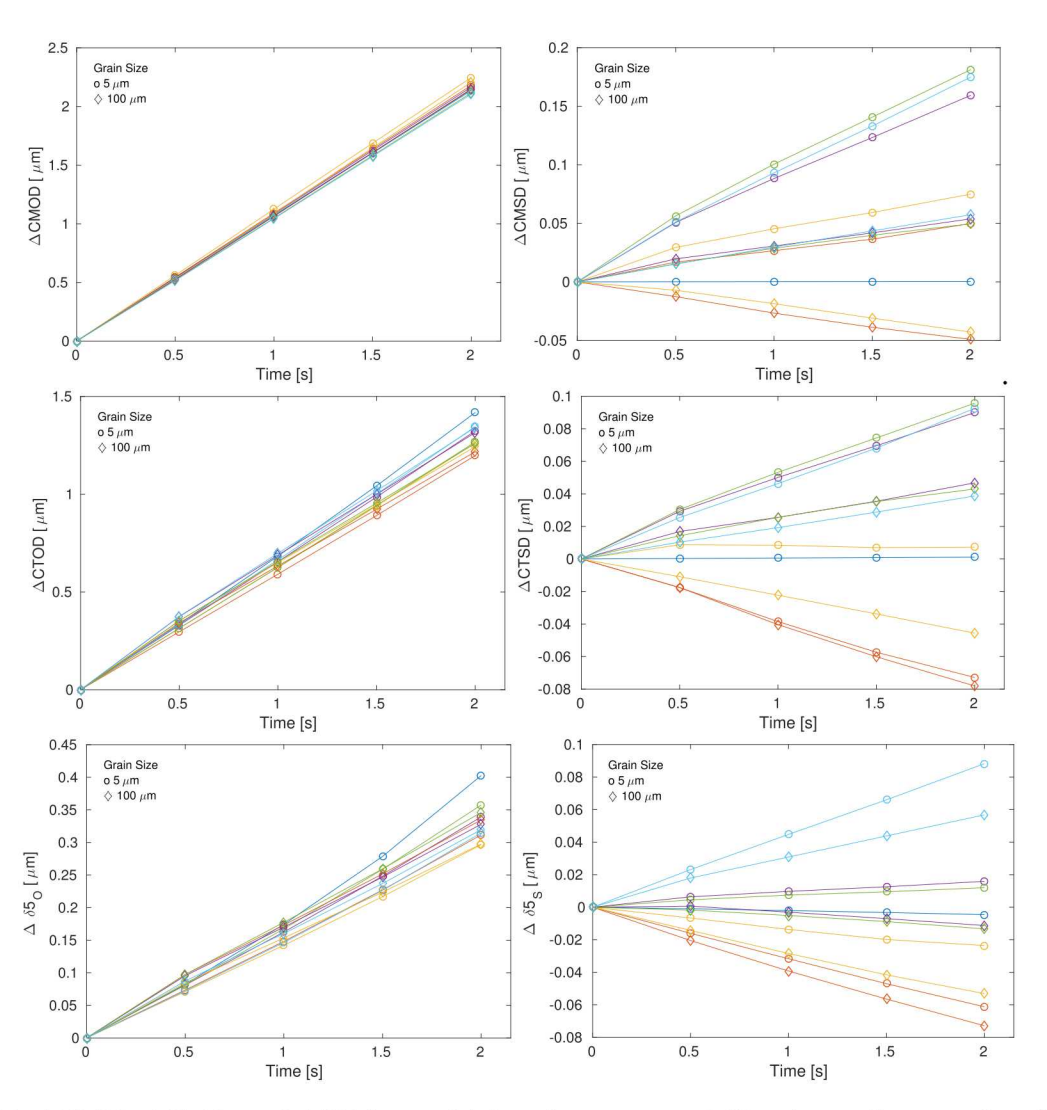


Figure 17: Δ CMD, Δ CTD, and $\Delta\delta$ 5 for multiple microstructural X-axis gradients under displacement control. Colors represent different microstructural realizations.

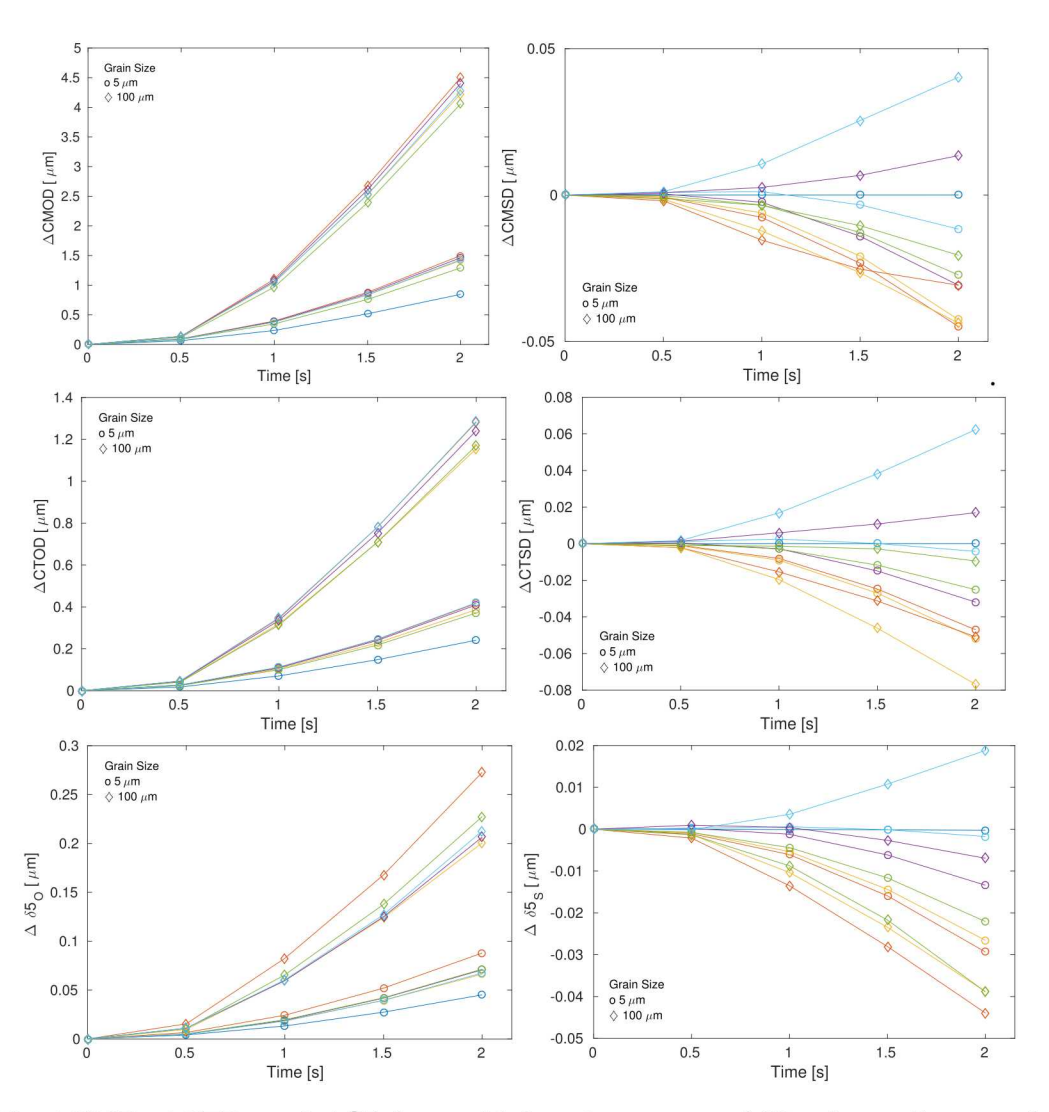


Figure 18: Δ CMD, Δ CTD, and $\Delta\delta$ 5 for multiple microstructural X-axis gradients under force control. Colors represent different microstructural realizations.

3.7 Results for texture gradients

This section presents the results using models with crystallographic texture presented in Figure 4 under force control. We consider crystallographic gradients along Y- and X-axis that goes from random orientation (no texture) to three single crystals orientations: [001], [011] and [111]. These orientations were chosen due to the high elastic anisotropy of Nickel (also stainless steel), which results in a strong difference in the elastic stiffness of single crystals. Indeed, the Young's modulus varies from 130GPa for crystals oriented along [001] to about 220GPa for crystals deformed along [011] and 290GPa for [111] orientation.

Figure 19 presents the evolution of the opening and sliding displacements for the same microstructure with different texture gradients under force control. These results show that in addition to the grain size and morphology, crystal orientations also have a significant effect on the fracture driving force variability. Interestingly, the sliding components may change their sign by only modifying the grain orientations.

To further investigate this finding we performed 10 realizations for texture gradients along the X-axis Y-axis and the results are presented in Figures 20 and 21, respectively. Clearly, the combination of texture and grain morphology increase the variability of the driving forces. Moreover, some cases seem to depend on the crystal orientations. Thus, we computed the distributions of normalized displacement at maximum load in box plots in Figures 22 and 23. The normalization factor is the corresponding opening displacement for [001] texture.

Although more statistics would provide more certainty, it seems that the mean $\Delta CMSD$ and $\Delta CTSD$ are biased towards positive values for texture gradients along the X-axis. Similarly, the $\Delta CMOD$ and $\Delta CTOD$ depend on the texture along Y-axis. The [111] orientation shows the lowest mean values while the [001] texture has the highest. These values correlate inversely with the elastic stiffness of the single crystals, which suggests that the mesoscale reduction of stiffness introduced by the texture can affect the fracture driving force; these effects justify a change about 5%. In the case of the $\Delta \delta 5$ for texture along Y-axis we do not observe a clear trend, which would suggest that the local grain orientation dominates this displacement.

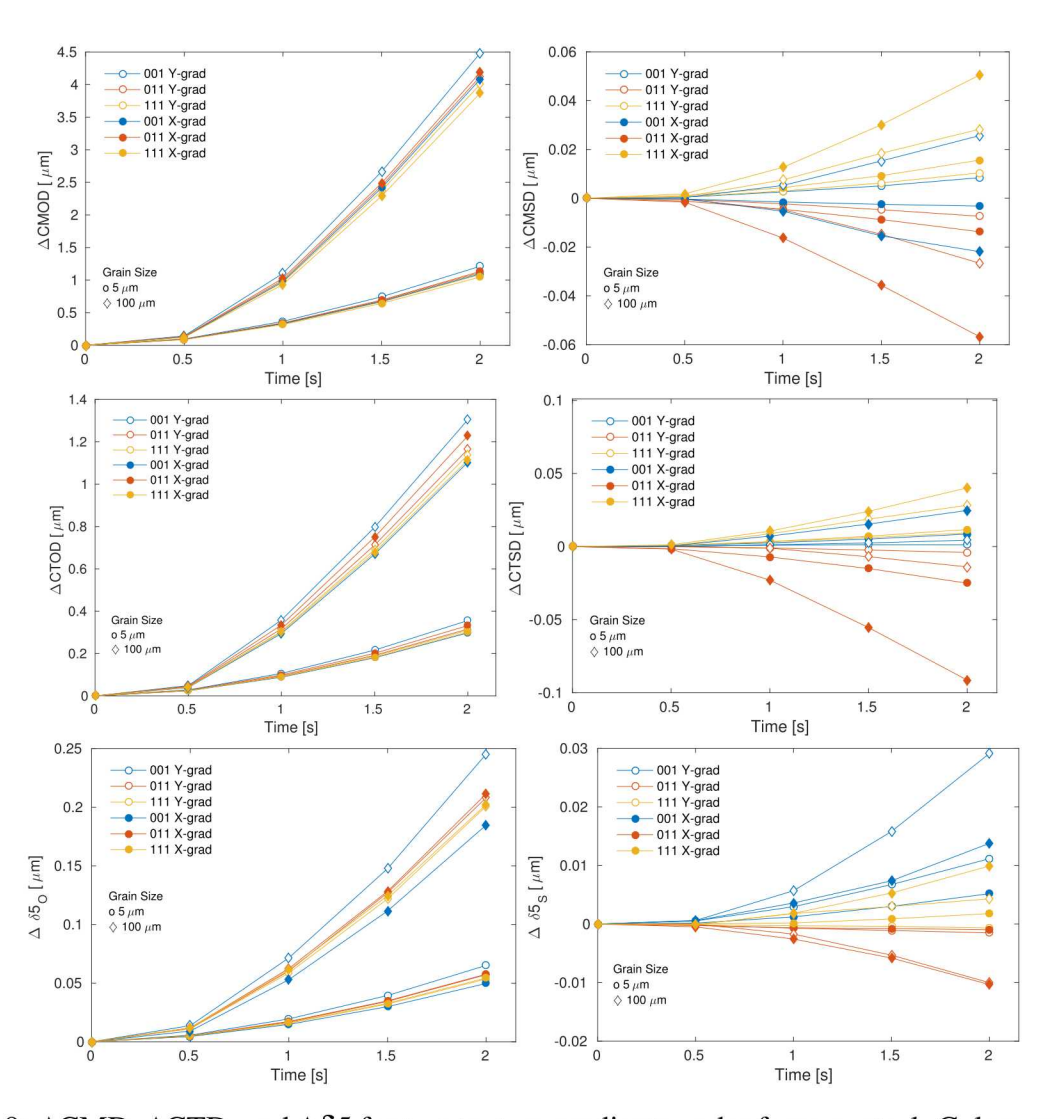


Figure 19: Δ CMD, Δ CTD, and $\Delta\delta$ 5 for two texture gradients under force control. Colors represent different microstructural realizations.

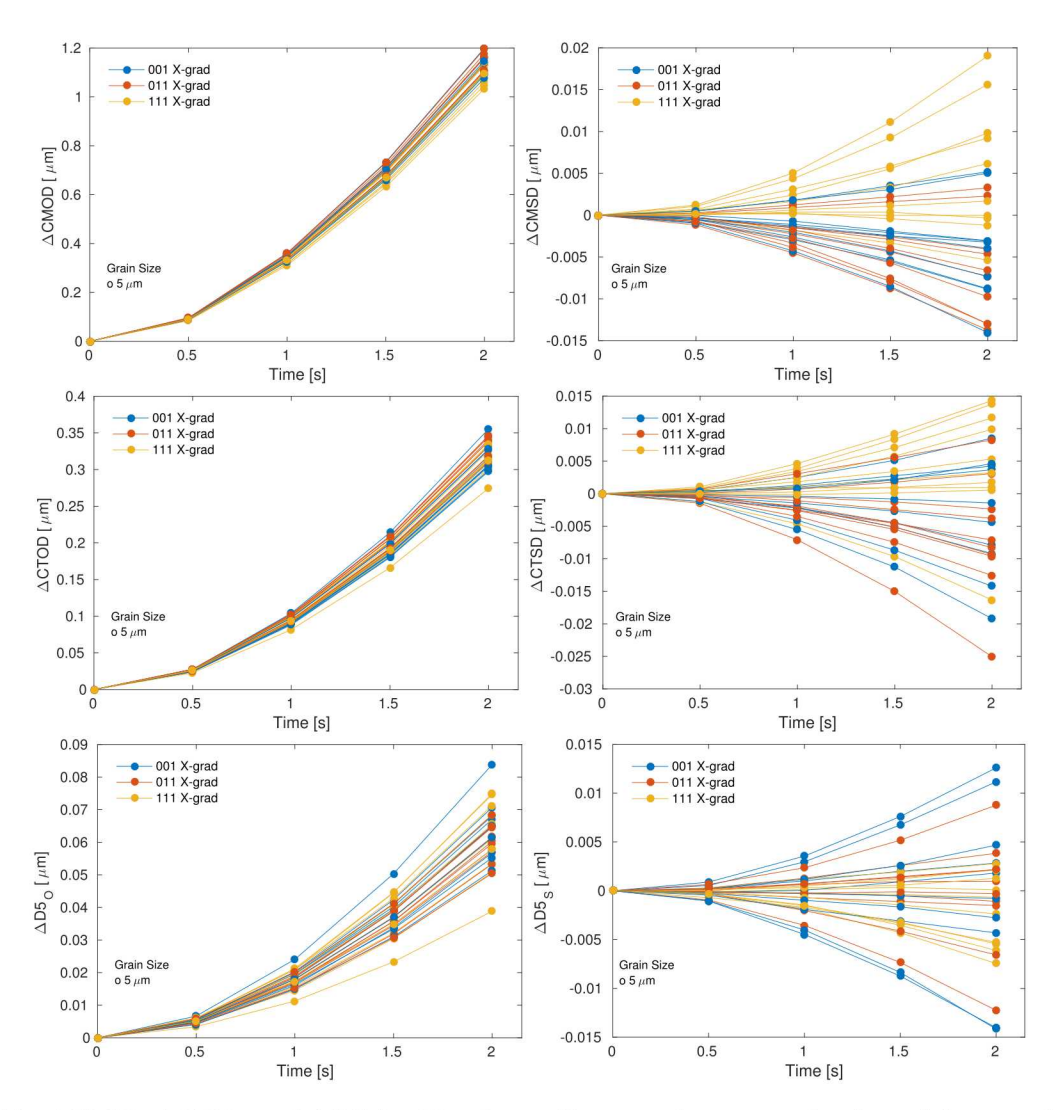


Figure 20: Δ CMD, Δ CTD, and $\Delta\delta$ 5 for X-axis gradients and mean grain size of $5\mu m$ under force control. Colors represent different microstructural realizations.

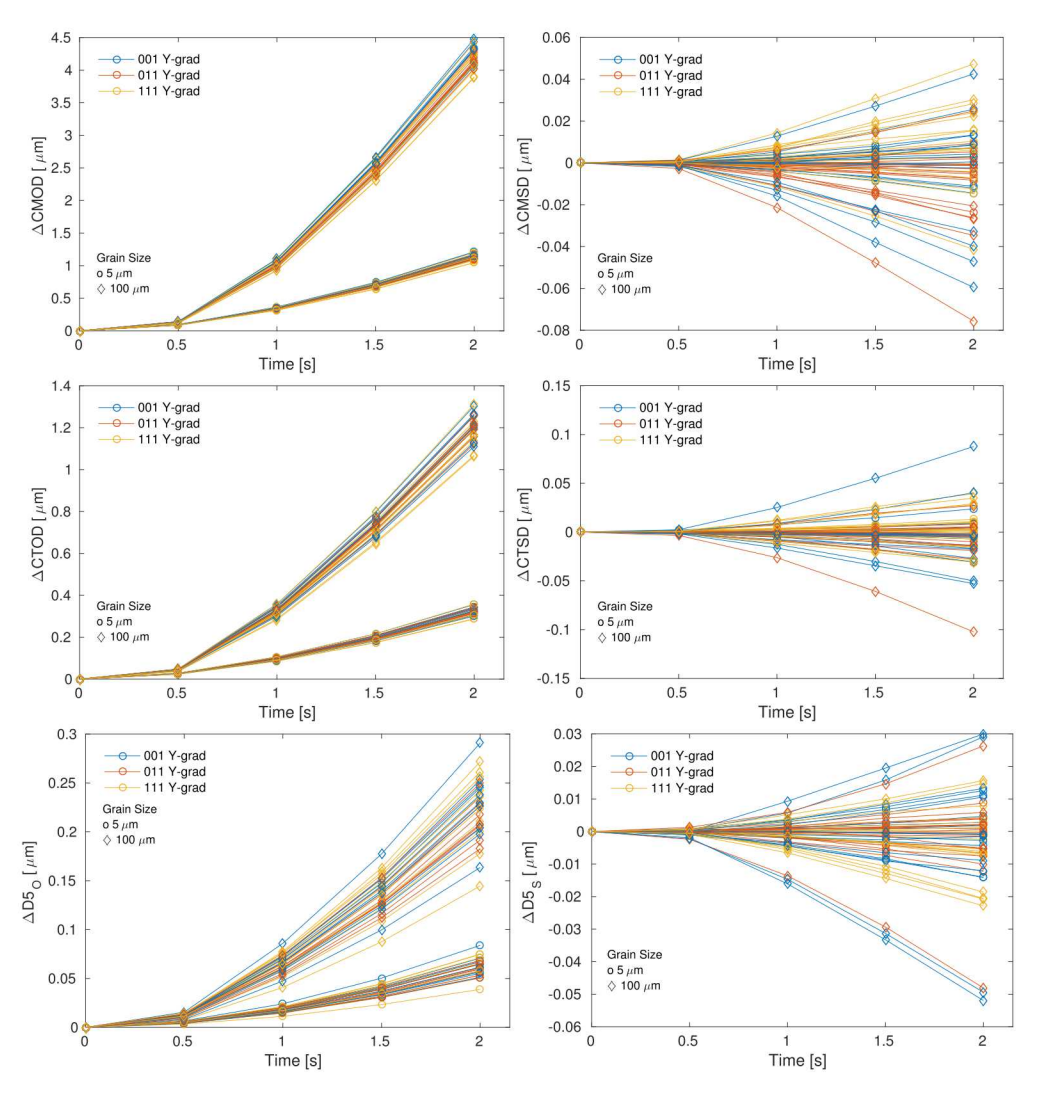


Figure 21: Δ CMD, Δ CTD, and $\Delta\delta$ 5 for Y-axis gradients under force control and two mean grain sizes. Colors represent different microstructural realizations.

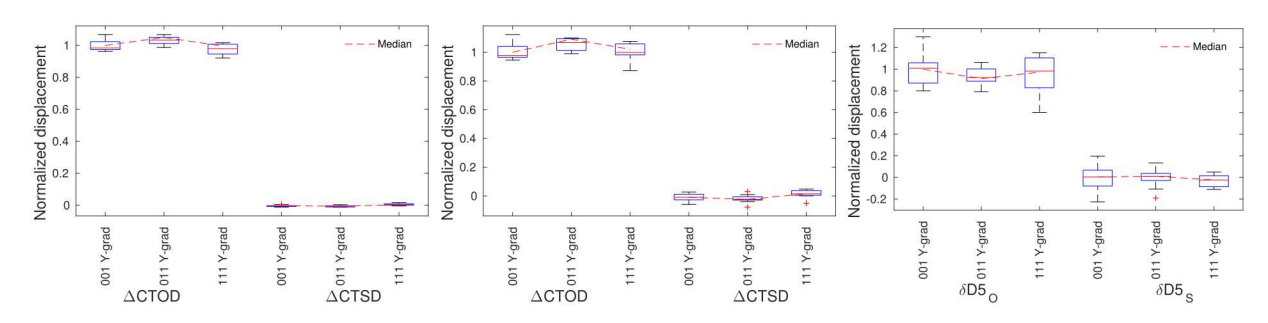


Figure 22: Boxplots summarizing normalized distributions of maximum Δ CMD, Δ CTD, and $\Delta\delta$ 5 values for multiple texture gradients along X-axis and mean grain size of $5\mu m$ under force control.

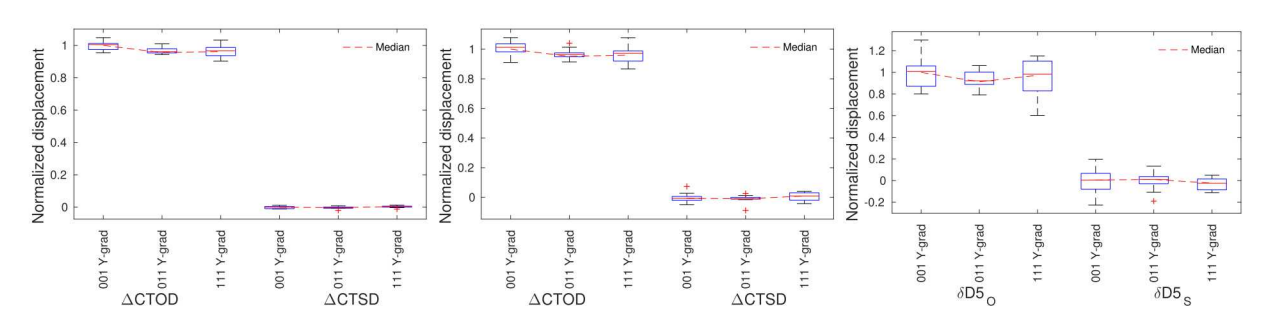


Figure 23: Boxplots summarizing normalized distributions of maximum Δ CMD, Δ CTD, and $\Delta\delta$ 5 values for multiple texture gradients along Y-axis under force control.

4 Plastic dislocation walls

Previous sections explored the effects of microstructure on fracture using a generic version of the constitutive model that can reproduce the macroscopic behavior of polycrystals. Indeed, we observed multiple effects, but it is difficult to point out a particular microstructural feature that controls the fracture toughness. For instance, Mode II is significant, but it is not clear what controls the direction of such shear (i.e., positive or negative $\Delta CTSD$). Most likely, this is controlled by the mesoscale neighborhood of the crack rather than the macroscopic (entire model) or local (each element) scales.

Such a dependence on the mesoscale has implications on the constitutive modeling requirements. Instead of just matching the macroscopic behavior, crystal plasticity models need to match the behavior of individual grains in order to make conclusion about mesoscale effects. Such a validation is rarely found in the literature and most the time it is incomplete. Furthermore, it is not entirely clear how to validate crystal plasticity approaches at a mesoscale, which is an engineering grand challenge.

In this research, we attempt a first order mesoscale validation by designing and implementing a constitutive model that matches single and poly-crystals. Indeed, this is the minimum requirement to predict local stresses and strains and very few models, if any, have been shown to reproduce flow behaviors of polycrystals and single crystals in multiple orientations. Next we present a modification of the constitutive model to consider the plastic deformation of dislocation structures. After that we perform various simulations to assess fracture toughness with this model.

4.1 Constitutive Formulation

The constitutive model presented in the previous section assumes that dislocation densities localize in elastic walls and soft channels; plastic deformation only occurs in channels, which are constrained by walls. This model is accurate at low stresses, but with increasing stress, walls may deform plastically. Thus, we implemented a model that allows for plastic deformation of the walls.

The shear rate has two terms, each for the channel and walls,

$$\dot{\gamma}^{\alpha} = \rho_{M}^{\alpha} l_{struct} b v_{G} \exp \left(-\frac{F_{0}}{k_{b}T} \left(1 - \left[\frac{\left\langle \left| \tau_{eff}^{\alpha M} \right| - S_{0}^{\alpha M} \right\rangle}{s_{t}^{0} \frac{C_{44}}{C_{44}^{0}}} \right]^{p} \right)^{q} \right) \operatorname{sgn} \left(\tau_{eff}^{\alpha M} \right) +$$

$$\rho_{W}^{\alpha} l_{struct} b v_{G} \exp \left(-\frac{F_{0}}{k_{b}T} \left(1 - \left[\frac{\left\langle \left| \tau_{eff}^{\alpha W} \right| - S_{0}^{\alpha W} \right\rangle}{s_{t}^{0} \frac{C_{44}}{C_{44}^{0}}} \right]^{p} \right)^{q} \right) \operatorname{sgn} \left(\tau_{eff}^{\alpha W} \right)$$

$$(15)$$

in which the subscripts M and W refer to mobile or wall, respectively. The athermal or threshold stress (S_0^{α}) is similar to Equation 2 with the corresponding mobile or wall dislocation densities.

Similarly, the dislocation density in the walls is computed following the balance rate in Equation 4, but without the cross slip term since we assume that walls are made of mostly of edge dislocations.

The effective stress of mobile dislocations $(\tau_{eff}^{\alpha})^M$ follows Equation 7 and the back stress is computed similarly to Equation 8. In the case of the walls, the effect stress $(\tau_{eff}^{\alpha})^W$ is defined by,

$$\tau_{eff}^{\alpha W} = \tau^{\alpha} + B^{\alpha} \tag{16}$$

in which the sign of the back stress is opposite to the case of mobile dislocations. The remaining magnitudes are identical except for Hill's accommodation factor that does not include a grain size dependence.

$$f_{Hill} = (1 - f_w) \frac{d\gamma^{\alpha}}{d\tau^{\alpha}} \tag{17}$$

Instead, the grain size dependence is introduce by the initial dislocation density, which affects the athermal stress and assuming that the initial structure size is $d_{struct}^0 \sim 1/\sqrt{\rho_M^0}$.

The material properties are almost identical to those in the previous section except for the initial dislocation densities. Single crystals are usually manufactured by melting and solidifying metals without any work hardening. This means that crystals are in an annealed state with very low dislocations densities. In contrast, upon rolling or other work hardening manufacturing processes, grain size are typically reduced and dislocation density can increase dramatically. Thus, we summarize prior history by specifying the initial grain size and dislocation density, which will also define the initial mean free path. We make the point that well annealed single and poly-crystals are less dependent on the initial conditions.

The macroscopic response from smooth specimens is presented in Figure 24 deformed at a strain rate of $0.001\%s^{-1}$. Here, we present four cases from experiments (full symbols) and experiments (continuous lines). These cases correspond to:

- Nickel single crystal with the loading oriented along the [111] direction from [18]. This configuration has the lowest possible maximum Schmid factor (0.27).
- Nickel single crystal with the loading oriented along the [001] direction from [19]. This configuration has the a maximum Schmid factor of 0.41 for eight slip systems.
- Polycrystalline rolled Nickel with the mean grain size of $2\mu m$. In m from [18]odels the initial dislocation densities are $\rho_M^0=1.5\times 10^{12}m^{-2}$ and $\rho_W^0=1.5\times 10^{13}m^{-2}$.
- Polycrystalline annealed Nickel with the mean grain size of $34\mu m$ from [20]. In models the initial dislocation densities are $\rho_M^0 = 2 \times 10^{11} m^{-2}$ and $\rho_W^0 = 2 \times 10^{12} m^{-2}$.

By validating single crystal macroscopic responses of models with experimental measurements, we increase the confidence at the mesoscale. Given that the development of a new constitutive model is not the main objective of this research, we argue that the agreement between models and experiments in Figure 24 is reasonable to proceed to compute fracture driving forces with more confidence. Nevertheless, future efforts should investigate constitutive models that reproduce single and polycrystals more accurately. Next, we present the results of notched specimens using this constitutive model. Note that the deformation rate in these simulations has been modified to match the experimental data used for validating the constitutive model.

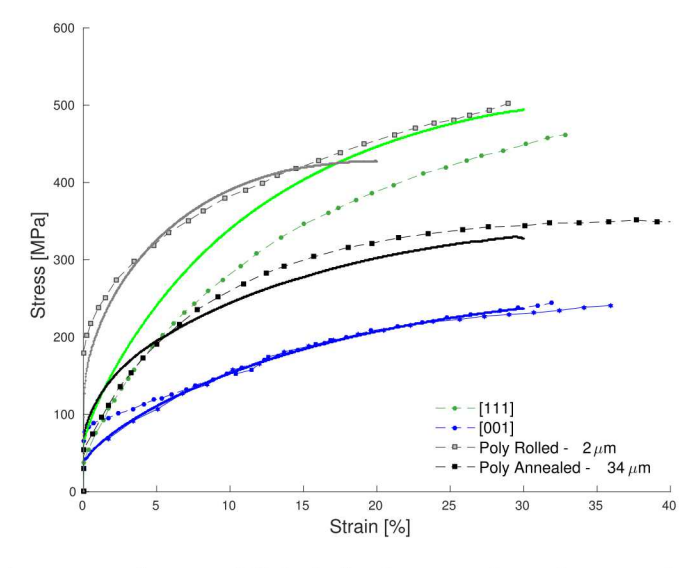


Figure 24: Stress-strain curves for two Nickel single crystals and two polycrystals from different manufacturers. Solid lines correspond to simulations while symbols correspond to experiments from the literature.

4.2 Results for equiaxed fine microstructures - Force control

Following the same path as in section 3.4 we adopt multiple realizations of the equiaxed fine microstructures using the constitutive model described in the previous section. Figure 25 presents the evolution of the opening and sliding displacements for such microstructures. Compared to the elastic walls results in Figure 7, the new constitutive model presents somewhat similar opening results in terms of mean values and spreads. Interestingly, even when both constitutive models show almost identical Δ CTOD, it seems that there is a difference in the variability of the Δ CTSD.

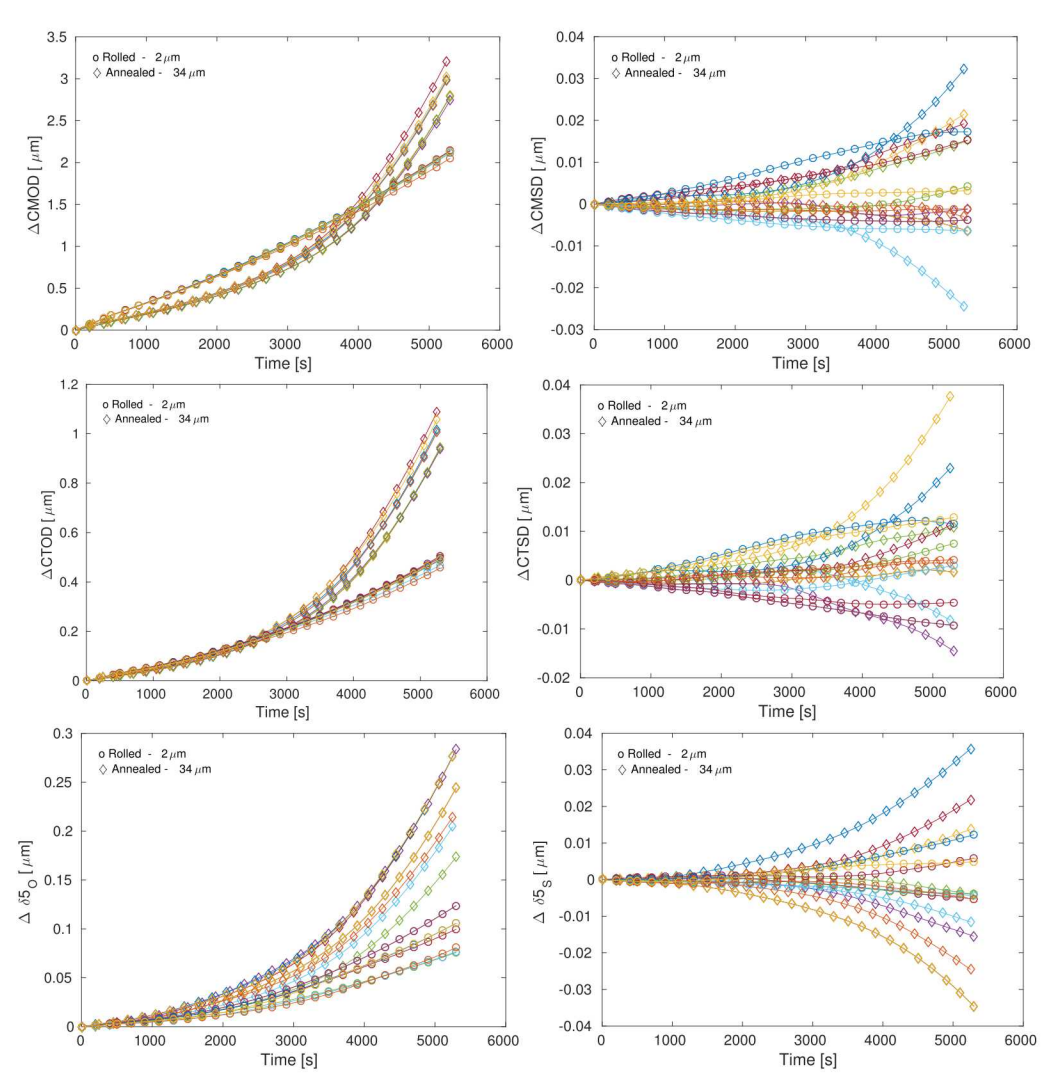


Figure 25: Δ CMD, Δ CTD, and $\Delta\delta$ 5 for multiple equiaxed microstructural realizations under force control. Colors represent different microstructural realizations.

4.3 Results for X-axis texture gradients - Force control

Figure 26 presents the evolution of the opening and sliding displacements for microstructures with texture gradients along the X-axis direction. The results are somewhat similar to those obtained with the elastic walls models in Figure 20. Furthermore, we computed the distributions of normalized displacement at maximum load in box plots in Figure 27. The normalization factor is the corresponding opening displacement for [001] texture.

Although the distributions overlap, , it seems that [111] orientation induces a positive shear component while [001] induces a negative shear components; this is specially noticeable for Δ CMSD and Δ CTSD. The opening components Similarly, the Δ CMOD and Δ CTOD depend on the texture along Y-axis. The [111] orientation show the lowest mean values while the [001] texture has the highest. These values correlates inversely with the elastic stiffness of the single crystals,

which suggests that the mesoscale reduction of stiffness introduced by the texture can affect the fracture driving force; these effects justify a change about 5%. In the case of the $\Delta\delta 5$ for texture along Y-axis we do not observe a clear trend, which would suggest that the local grain orientation dominates this displacement.

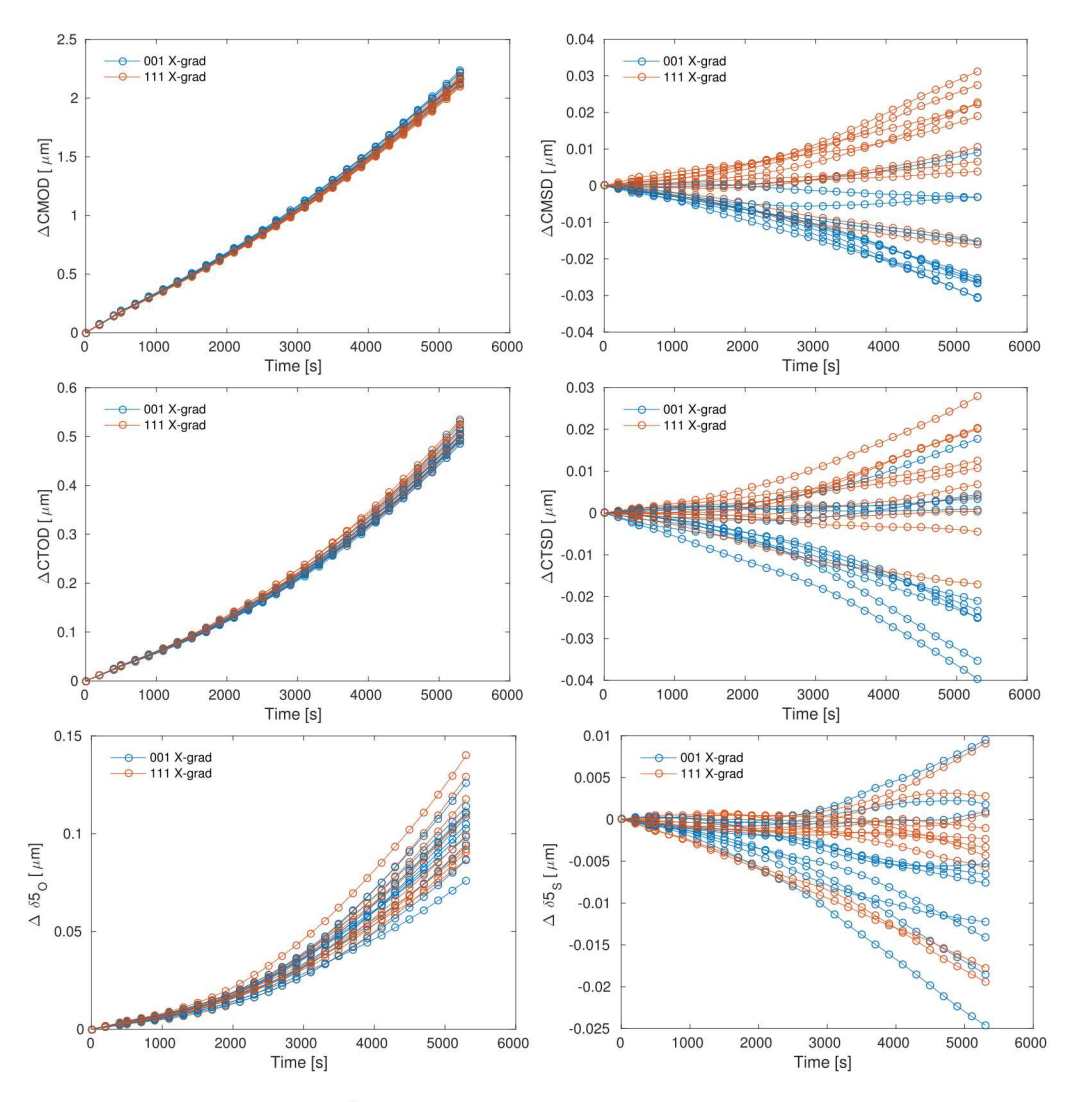


Figure 26: Δ CMD, Δ CTD, and $\Delta\delta$ 5 for X-axis gradients and mean grain size of $2\mu m$ under force control. Colors represent different microstructural realizations.

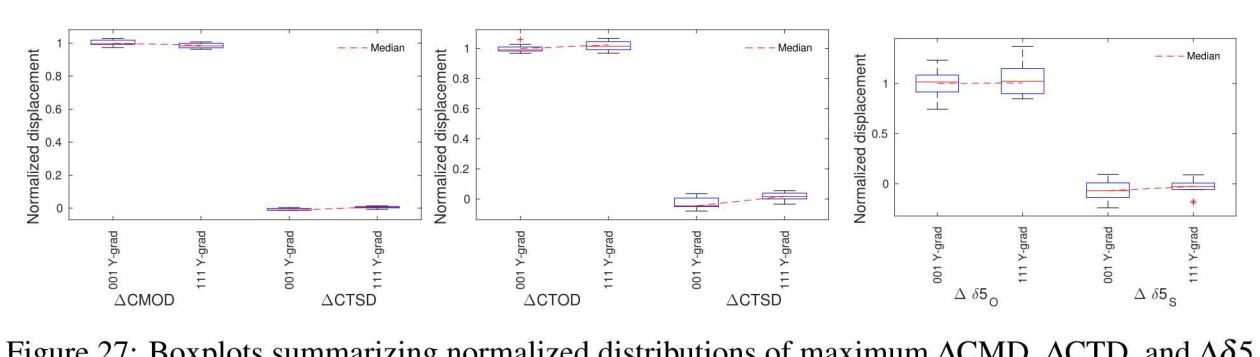


Figure 27: Boxplots summarizing normalized distributions of maximum Δ CMD, Δ CTD, and $\Delta\delta$ 5 values for multiple texture gradients along X-axis under force control.

5 Discussion and Conclusions

The introduction of microstructural variability propagates intro fracture driving force in multiple ways. Furthermore, microstructural morphology, gradients and texture contribute independently and significantly to the fracture driving forces, which makes it difficult to identify one specific feature that dominates the response. Instead, we identified various general characteristics:

- The microstructural variability has different effects on the multiple driving forces considered. Thus, propagation of uncertainty is specific to each fracture driving force measure.
- Equiaxed microstructures show almost no impact on Δ CMOD variability, for which homogeneous J2 and microstructure-sensitive simulations are almost identical; on the contrary, Δ CTOD and $\delta 5_O$ are affected by the microstructure. Hence, standardized CTOD measurements based on CMOD plastic hinge may smear out the driving force variability.
- The sensitivity of the fracture driving force to the microstructure increases as the measurement of the driving force approaches the crack tip. Thus Δ CMOD is less sensitive than Δ CTOD and δs_O . Furthemore, the normalized Δ CMSD is negligible compared to Δ CTSD and δs_O and suggests that Mode II is intrinsically introduced by microstructure. Hence, experimental fracture toughness measurements based on plastic hinge model [1] should be regarded as less sensitive to intrinsic fracture variability.
- The incorporation of the microstructure induces a significant Mode II compared to homogenized models. For random grain morphology and orientation, shear occurs in both directions, which effectively compensates shear growth on a macroscopic scale and allows cracks to grow, *in average*, in Mode I. Microstructural gradients can induce Mode II displacement along a preferential direction, which has the potential to turn the crack path as observed in experiments (e.g., [21]).
- The microstructural attributes in the neighborhood of the crack tip seem to control a significant fraction of the variability. More statistics are necessary to understand and quantify the size of the neighborhood in relation to the mean grain size and the CTOD. Since the CTOD changes as a function of the loading level, it is plausible that such a neighborhood is also a function of the applied load.
- The variability of the driving forces is increased by the introduction of microstructural gradients. Both local and long range gradients may affect, but the former would not affect CMOD.
- Mesoscale texture gradients may also affect the driving force. Long range gradients seem to have a secondary effect while local texture may have a larger impact.

5.1 What is next?

Future efforts should focus on linking the mesocale to the macro and micro scales. For instance, further research could estimate quantitatively the effect of microstructure on the methodology stipulated by ASTM E1820 standard for measuring fracture toughness. This research would require modeling the exact fracture specimens and loading conditions imposed by the standard. Following the guidance from this report, further investigation may identify unsafe or unreliable predictions for certain materials, best manufacturing practices to improve fracture toughness certification and better practices for the standard.

A more robust link between the mesoscale with the macroscopic scale is key to bring understanding from atomistic models into engineering applications. We envision that CTD is an ideal mesoscale magnitude to facilitate the handshake between atomistic and engineering fracture toughness. Indeed, atomistic simulations could investigate the role of the environment and crystallographic orientation on CTD, which may be inferred from the macroscopic applied state though mesoscale correlations.

References

- [1] T. L. Anderson, Fracture Mechanics: Fundamentals and Applications, 3rd Edition, CRC Press, 2004.
- [2] Materials genome initiative. www.mgi.gov.
- [3] A. White, The materials genome initiative: One year on, MRS Bulletin 37 (8) (2012) 715716.
- [4] F. O. Riemelmoser, R. Pippan, The j-integral at dugdale cracks perpendicular to interfaces of materials with dissimilar yield stresses, International Journal of Fracture 103 (4) (2000) 397–418.
- [5] O. Kolednik, J. Predan, G. Shan, N. Simha, F. Fischer, On the fracture behavior of inhomogeneous materials case study for elastically inhomogeneous bimaterials, International Journal of Solids and Structures 42 (2) (2005) 605 620.
- [6] N. K. Simha, F. D. Fischer, O. Kolednik, J. Predan, G. X. Shan, Crack tip shielding or antishielding due to smooth and discontinuous material inhomogeneities, International Journal of Fracture 135 (1) (2005) 73–93.
- [7] ASTM E1820-09 Standard test method for measurement of fracture toughness. (2009).
- [8] H. Schwalbe K, Introduction of d5 as an operational definition of the ctod and its practical applications, in: W. G. Reuter, J. H. Underwood, J. C. Newman (Eds.), Fracture Mechanics: 26th Volume, STP 1156, ASTM, 1997, pp. 763–778.
- [9] R. J. Asaro, Micromechanics of Crystals and Polycrystals, in: John W. Hutchinson and Theodore Y. Wu (Ed.), Advances in Applied Mechanics, Vol. Volume 23, Elsevier, 1983, pp. 1–115.
- [10] A. Khan, S. Huang, Continuum theory of plasticity, Wiley, New York, 1995.
- [11] ABAQUS, FEM software V6.14, Simulia Corp., Providence, RI, USA (2016).
- [12] G. M. Castelluccio, Progress in modeling hydrogen effects in cyclic plasticity, Tech. Rep. SAND2016-5879R, Sandia National Laboratories (2016).
- [13] D. Kuhlmann-Wilsdorf, Theory of plastic deformation: properties of low energy dislocation structures, Materials Science and Engineering: A 113 (1989) 1–41.
- [14] D. Kuhlmann-Wilsdorf, The theory of dislocation-based crystal plasticity, Philosophical Magazine A 79 (4) (1999) 955–1008.
- [15] U. F. Kocks, A. Argon, M. F. Ashby, Thermodynamics and kinetics of slip, Progress in Materials Science 19.
- [16] U. F. Kocks, H. Mecking, Physics and phenomenology of strain hardening: the FCC case, Progress in Materials Science 48 (3) (2003) 171–273.

- [17] M. Sauzay, L. Kubin, Scaling laws for dislocation microstructures in monotonic and cyclic deformation of fcc metals, Progress in Materials Science 56 (6) (2011) 725–784.
- [18] D. Kuhlmann-Wilsdorf, Chapter 59 The LES theory of solid plasticity, in: F.R.N. Nabarro and M.S. Duesbery (Ed.), Dislocations in Solids, Vol. Volume 11, Elsevier, 2002, pp. 211–342.
- [19] V. A. Starenchenko, D. V. Lychagin, R. V. Shaekhov, . V. Kozlov, Action of test temperature on evolution of dislocation structure of nickel single crystals with the [001] compression axis, Russian Physics Journal 42 (7) (1999) 653–659.
- [20] S. S. Satheesh Kumar, T. Raghu, Mechanical behaviour and microstructural evolution of constrained groove pressed nickel sheets, Journal of Materials Processing Technology 213 (2) (2013) 214–220.
- [21] G. M. Castelluccio, J. E. Perez Ipina, A. A. Yawny, H. A. Ernst, Fracture testing of the heat affected zone from welded steel pipes using an in situ stage, Engineering Fracture Mechanics 98 (2013) 52–63.

DISTRIBUTION:

1	MS 0346	Diane Peebles, 01556
1	MS 0840	Joseph Bishop, 01554
1	MS 0840	Brad Boyce, 01851
1	MS 0840	Edmundo Corona, 01554
1	MS 0840	John Emery, 01556
1	MS 0840	Eliot Fang, 01554
1	MS 0840	David Littlewood, 01444
1	MS 0840	Pania Newell, 01555
1	MS 0840	James Redmond, 01550
1	MS 0840	Benjamin Reedlun, 01554
1	MS 0840	William Scherzinger, 01554
1	MS 0889	Corbett Battaile, 01814
1	MS 0889	Dave Reedy, 01556
1	MS 1411	Hojun Lim, 01814
1	MS 1411	Amy Sun, 01814
1	MS 1415	Gustavo Castelluccio, 01556
1	MS 8256	James Foulk III, 08256
1	MS 0899	Technical Library, 09536

